Modeling deep control pulsing flux of native H_2 throughout tectonic fault-valve systems

F.V. Donzé[1], L. Bourdet[1], L. Truche[1], C. Dusséaux[2] and P. Huyghe[1]

[1] Université Grenoble Alpes, University Savoie Mont Blanc, CNRS, IRD, IFSTTAR, laboratoire ISTerre, 38000 Grenoble, France;

[2] Université de Bourgogne-Franche-Comté, Laboratoire Chrono-environnement, 25030 Besançon, France;

Corresponding author: Frédéric Victor Donzé (`Frederic.donze@univ-grenoble-alpes.fr`)

Key points

- The pulsing flow of natural H_2 along a fault is simulated with a numerical model.
- The H_2 pulses are generated in presence of contrasted stress-dependent permeability zones at depth.
- The periodicity of the H_2 pulses is of the order of several months.

Abstract. Pulsing seepages of native hydrogen (H_2) have been observed at the surface on several emitting structures. It is still unclear whether this H_2 pulsed flux is controlled by deep migration processes, atmosphere/near-surface interactions or by bacterial fermentation. Here, we investigate mechanisms that may trigger pulsating fluid migration at depth and the resulting periodicity. We set up a numerical model to simulate the migration of a deep constant fluid flow. To verify the model's formulation to solve complex fluid flows, we first simulate the morphology and amplitude of 2D thermal anomalies induced by buoyancy-driven water flow within a fault zone. Then, we simulate the H_2 gas flow along a 1-km draining fault, crosscut by a lower permeable rock layer to investigate the conditions for which a pulsing system is generated from a deep control. For a constant incoming flow of H_2 at depth, persistent bursts at the surface only appear in the model if: (I) a permeability with an effective-stress dependency is used, (II) a strong contrast of permeability exists between the different zones, (III) a sufficiently high value of the initial effective stress state at the base of the low permeable layer exists, and (IV) the incoming and continuous fluid flow of H_2 at depth remains low enough so that the overpressure does not "open" instantly the low permeability layer. The typical periodicity expected for this type of valve-fault control of H_2 pulses at the surface is at a time scale of the order of 100 to 300 days.

Key words: Natural hydrogen, fluid migration, H_2 pulses, fault-valve system, numerical modeling

1 Introduction

Continental gas seepages containing abnormally high concentrations of native hydrogen (H_2) can be observed at the surface, either in soil gases from several emitting structures (e.g. "fairy circles") or dissolved in water springs located along deep and draining fault systems (e.g. Larin et al., 2015; Zgonnik et al., 2015; Prinzhofer et al., 2019; Donzé et al., 2020b; Lefeuvre et al., 2021, 2022; Frery et al., 2021). Provided that H_2 is produced at depth, several geological processes have been proposed for H_2 generation, considering that some of them may operate simultaneously (Truche et al., 2020). Among them, one can cite (I) serpentinization of ultramafic rocks in ophiolitic complexes, komatiite and ultramafic intrusions, mantle xenoliths (Beinlich et al., 2018), and more generally rocks containing ferrous iron (Fe), (II) radiolysis of water during radioactive decay of uranium (^{235}U), thorium (^{228}Th) and potassium (^{40}K) in host rocks (Lin et al., 2005), and (III) mantle and core degassing (Gilat & Vol, 2012).

Alteration processes involving hydration of ultrabasic rocks induce a density decrease as the solid fraction expands at low confinement (Zheng et al., 2018). In a confined system, expansion generates stress that can fracture the rock and increase its porosity and permeability (Zhang et al., 2019) enabling H_2 migration. Indeed, foliated serpentinite are often crosscut by veins that are frequently folded and deformed, suggesting that hydrofracturing occurred synchronously with a distributed deformation in the rock matrix (Tarling et al., 2019). This overpressure development and hydrofracturing could be at the origin of swarms of seismic events observed in the surrounding rock mass due to stress transfer, which reactivates shear fractures. An enhanced seismic activity has been observed at different H_2-seeping locations. For example, the important seismic activity to the south of the North Pyrenean Fault beneath the Mauléon Basin (western Pyrenees) has been linked to possibly active serpentinization processes related to a massive mantle body detected at shallow depth (< 10 km; Lefeuvre et al., 2021, 2022). Souriau et al. (2014) interpret these earthquake clusters as related to convective fluid circulation along the North Pyrenean Fault. Several studies also interpret these seismicity patterns as the result of stress triggered by fluid flow (e.g. Faulkner et al., 2010; Hainzl, 2004; Hardebeck, 2012). Regarding their temporal aspects, which could contribute to generate bursts of H_2 emission at the surface, it appears that the seismic activity occurs with no clear temporal periodicity over a time of 60 years in the Pyrenees (Sylvander et al. 2021). The seismic activity of other serpentinization contexts is characterized by strong releases of energy followed by protracted (hundreds of years) intervals of quiescence (e.g. Palaeozoic basement of southeastern Sicily; Giampiccolo et al., 2017). However serpentinization and radiolysis of water under the effect of ionizing radiation produced by the radioactive decay of radiogenic nuclides do not appear the only mechanisms capable to produce H_2 in the continental crust. A recent exploration of paleofluids trapped in some Precambrian crystalline rocks for more than a billion years has revealed surprisingly high concentrations of hydrogen and methane with no apparent connection to these ultramafic rocks

(e.g. Outokumpu borehole in Finland, Kola superdeep borehole in Russia or Kid Kreek Mine in Canada) (Kietäväinen et al., 2013; Scherwood Lollar et al., 2017; Truche et al., 2022).

A deep origin for observed surface H_2 seepages implies fluid flow through fracture systems within the H_2-producing zone (Lin et al., 2005; Zhang et al., 2019), followed by fluid migration along major draining pathways, i.e. tectonic faults. However, the flow should be high enough to avoid the total consumption of H_2 by abiotic or microbially-mediated redox reactions. At temperatures above 100-150°C, H_2-consuming abiotic processes involve thermochemical sulfate reduction (Truche et al., 2009), pyrite reduction into pyrrhotite (Truche et al., 2010, 2013), and/or CO_2/CO reduction into methane and other hydrocarbons via a Fischer-Tropsch-Type processes (FFT) (Ellison et al., 2021). At lower temperatures (<120°C), i.e. closer to the surface, microbially-mediated redox reactions and/or adsorption represent the main processes of H_2 consumption (Lin et al., 2005; Truche et al., 2018). There, many microbial communities, such as bacteria, archaea and eukaryotes, possess hydrogenase-encoding genes and can use H_2 as a source of energy (Myagkiy et al., 2019, Ménez, 2020). These reactions being in part controlled by hydrogen availability and its behavior in presence of water (Monnin et al., 2021), H_2 solubility and vapor–liquid partitioning remains a key information regarding H_2 systems (Bazarkina et al., 2020) due to hydrogen low solubility in pure water and even lower in brine (Chabab et al., 2020). Thus, depending on the pressure and temperature conditions, H_2 in gaseous form can easily interact with its environment, which impact greatly its lifetime during migration. Associated to external factors such as near-surface atmospheric pressure variations or Earth tides, these biogeochemical sinks for H_2 may explain the daily periodicity of H_2 bursts that last for 6 hours observed in "fairy circles" emitting structures located in the Minas Gerais State (Brazil) (Moretti et al., 2021; Myagkiy et al., 2019).

All the above abiotic or microbially-induced H_2-consuming reactions occur under kinetic control conditions. Therefore, a rather quick fluid migration promotes the preservation of dissolved or gaseous H_2. However, water circulation is limited in highly permeable and saturated fault zones at hydrostatic pressure, resulting in a relative low gas permeability. Therefore, the presence of large thermal or chemical gradients appears essential to generate significant flow in presence of water. At great depths in poorly permeable rocks, the temperature increase or fluid accumulation below a low-permeability rock layer can lead to fluids overpressure and escape through fluid fault opening as the fluid pressure approaches the minimum in-situ stress. Hence, low permeable rock layer can act as fluid barriers, which can eventually result in a fault-valve system generating episodic but regular bursts of natural hydrogen at the surface.

The objective of the present study is to address the required conditions at depth (fluid pressure and in-situ stress) along a fault obstructed by a low permeable layer (thickness, depth, and permeability) to generate a H_2 pulsing system at the surface. Based on an open-source software for reservoir modelling and sim-

ulation (MRST), we set up a numerical model to simulate H_2 flow along a fault using Darcy's law. This model takes into account the contribution of the in-situ effective stress along the fault to the permeability changes and the effect of the temperature and pressure gradients on the fluid density and viscosity.

First, we simulate the morphology and amplitude of 2D thermal anomalies induced by buoyancy-driven flow of water only within fault zones to check the numerical model formulation since no reference H_2 migration models along a fault have been developed so far. Nevertheless, hydrothermal convection triggered by buoyancy effects creates complex thermal anomalies whose morphology and amplitude are difficult to model, especially when considering depth- and time-dependent permeability. This type of convection has been studied by Guillou-Frottier et al. (2020) using the Comsol Multiphysics™ software who showed that only proven and effective softwares are able to simulate such complex flow patterns. We compare their results with the ones we obtained with MRST.

Second, we set up a reference model configuration producing a H_2 pulsing system at the surface while the basal incoming flow rate of H_2 at depth (1 km) is kept constant. The model takes into account the presence of a low-permeability layer crossing the fault at a given depth. Based on this configuration, we present a parametric study to characterize the evolution of flow rate at the surface depending on several parameters, e.g. incoming flow rate, depth, thickness, permeability and in-situ stress state. We show that the use of an effective stress-dependent permeability (Donzé et al., 2020a) for the low permeable layer can generate such pulsing system.

2 Modeling fluid flow along the fault and associated driving forces

Tectonic faults are composite systems consisting of a high strain zone called the 'fault core' surrounded by a lower strain zone called the 'damage zone'. In the fault core, the fragmentation of the original bedrock material leads to the formation of a gouge, and implies strong mechanical and geochemical modifications due to e.g. fluid-rock interactions (Fossen, 2020). Thus, fluid upward migration across the fault zone is limited by the low permeability of the fault core acting as an impermeable barrier (Wibberley et al., 2008). However, the damage zone is characterized by a lower level of deformation, and exhibits numerous connected fractures or secondary faults (Figure 1). In low-impermeable rocks, the damage zone as well as the interface in-between the core and the damage zone are of main interest because they represent preferential pathways for fluids migration along faults over long distances (Henry et al., 2019; Tsopela et al., 2019). Indeed, geothermal fluid activity i.e. hot springs (>250°C) and seeps are commonly located within structurally complex zones in a fault array (e.g. geothermal fields in fault step-overs in a segmented rift system in New Zealand;

Rowland and Sibson, 2004; or along a segmented fault in France; Taillefer et al., 2017). Based on the ability of large tectonic faults to drain water and associated solutes from deep zones to the surface, we consider them as the main driving flow pathway for the fluids in our model.

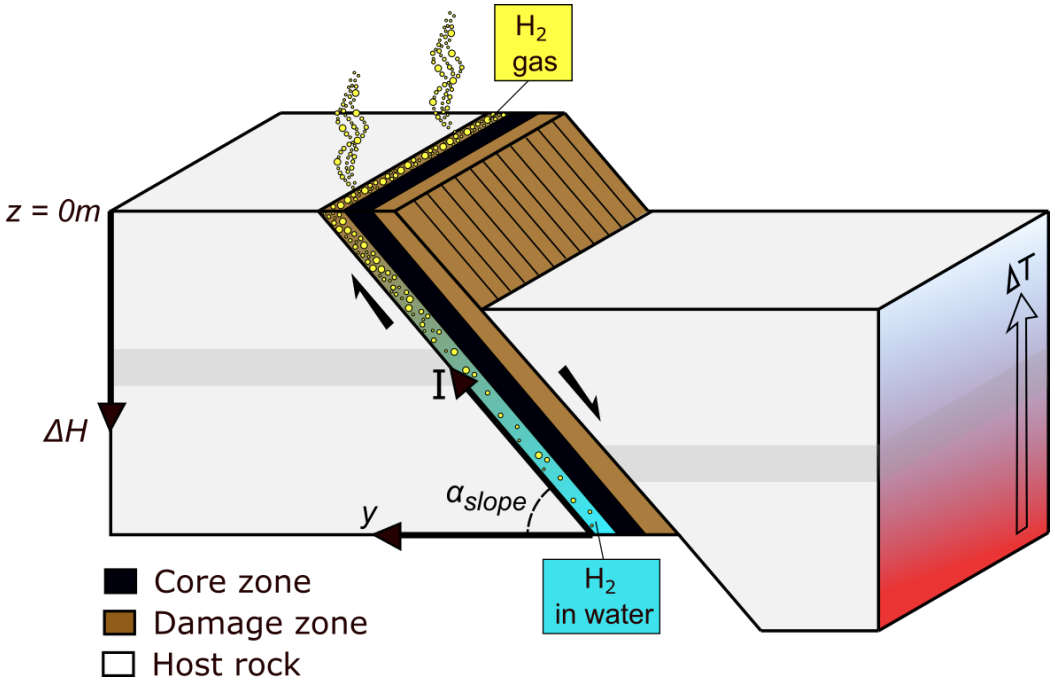

@ >p(- 0) * @

Figure 1. Schematic vertical cross-sectional view of a normal fault of height H, including the core and the damage zones. Fluids can migrate upwards at the interface core-damage zones and within the damage zone (brown colored zone) where fractures are highly connected. A temperature gradient ΔT or fluid over-pressure can be major driving mechanisms for fluid flow.

2.1. Fluid flow model

Modelling multiphase flow is challenging as phase transitions needs to be taken into account. First, we consider the damage zone as an equivalent porous medium, i.e. a highly connected set of fractures formed as a continuum with homogeneous hydraulic properties. Second, we use Darcy's law considering that fluid flow along the fault is stationary with small inertial forces compared to viscous forces. The equations system used to describe multiphase flow consists of nonlinear conservation laws, constitutive laws and coupled properties (saturation, molar fractions, etc.). Taking into account the potential presence of both water and dihydrogen along the fault, we use a fully coupled model with two-phase (Liquid and gas), two-component (H_2O and H_2), non-isothermal and

miscible flow as proposed by Lauser et al., (2011), the liquid phase being considered as the wetting phase.

2.1.1 Conservation Equation

The transient distribution of mass and energy at every point in space along the fault is described by a general balance equation such as,

$$\frac{}{\mathrm{t}} + \nabla \bullet \Psi = Q \quad (1)$$

with a storage term ξ, a flux term Ψ and a source term Q. This balance equation is applied to both water and dihydrogen.

Mass conservation for these two components, is given by the following set of equations:

$$\xi = \varphi \sum_{\alpha=l,g} \left(\rho_{mol,\alpha}\ \chi_{\alpha}^{\kappa}\ \mathrm{S}_{\alpha}\right) \quad (2)$$

$$\Psi = -\sum_{\alpha=l,g} \left(\rho_{mol,\alpha}\ \ {}_{\alpha}^{\kappa}\ \mathrm{v}_{\alpha} + D_{pm,\alpha}^{\kappa}\ \ {}_{mol,\alpha}\ \nabla\chi_{\alpha}^{\kappa}\right) \quad (3)$$

$$\mathbf{v}_{\alpha} = \mathbf{v}_{\alpha}^{\kappa=H2O,H2} \quad (4)$$

$$\rho_{mass,\alpha} = \rho_{mol,\alpha} \sum_{\kappa=H2O,\ H2} \left(\chi_{\alpha}^{\kappa}\ M^{\kappa}\right) \quad (5)$$

$$Q_{\alpha}^{\kappa} = \sum_{\alpha=l,g} \left(\rho_{mol,\alpha}\ \ {}_{\alpha}^{\kappa}\ q_{\alpha}\right) \quad (6)$$

For each phase $= l, g$, (l for liquid and g for gas), and components $= \mathrm{H}_2$ or $\mathrm{H}_2\mathrm{O}$, the quantities used in equations 2-6 are defined in Table 1.

Table 1. List of physical quantities used in equations 2-6

φ	Equivalent porosity of the fault damage fault zone
$\rho_{\alpha,mass}$	Mass density of the phase
χ_{α}^{κ}	Mole fraction of a component in the phase
v_{α}	Specific heat capacity of the solid phase
S_{α}	Saturation of phase
$D_{pm,\alpha}^{\kappa}$	Molecular diffusion coefficient of component
M^{κ}	Molar mass of component
q_{α}	Mass source term of component

Regarding the conservation of energy, the corresponding equations are,

$$\xi = \varphi \sum_{\alpha=l,g} \left(\rho_{mass,\alpha} U_{\alpha} S_{\alpha}\right) + (1-\varphi)\rho_s C_S T \quad (7)$$

$$\Psi = -\sum_{\alpha=l,g} \left(\frac{k_{\mathrm{r}}}{\mu_{\alpha}} \rho_{mass,\alpha}\ h_{\alpha}^{\kappa}\ \mathbf{v}_{\alpha}\right) - \sum_{\kappa=H2O,H2} \sum_{\alpha=l,g} \left(D_{pm,\alpha}^{\kappa} \rho_{mol,\alpha} h_{\alpha}^{\kappa} M^{\kappa} \nabla\chi_{\alpha}^{\kappa}\right) - \lambda_{\mathrm{pm}} \nabla T \quad (8)$$

$$Q = q^h \quad (9)$$

For each phase $= l, g$, (l for liquid and g for gas), and the components $= \mathrm{H}_2$ or $\mathrm{H}_2\mathrm{O}$, the quantities used in equations 7-9 are defined in Table 2.

Table 2. List of physical quantities used in equations 2-6

U_α	Specific internal energy of phase
ρ_s	Density of the solid phase
C_S	Specific heat capacity of the solid phase
T	Temperature
k_{r}	Relative permeability of phase
μ_α	Viscosity of phase
h_α^κ	Specific enthalpy of phase
λ_{pm}	Heat conduction coefficient
q^h	Mass source term of component

2.1.2 Constitutive relations

As stated previously, the velocity of the liquid or gas phase $\mathbf{v}_\alpha$ is assumed to be described by the Darcy law, such as,

$$\mathbf{v}_\alpha = \frac{K_\alpha}{\mu_\alpha}\left(\nabla P_\alpha - \rho_{mass,\alpha}\mathbf{g}\nabla z\right) \quad (10)$$

Where $\mathbf{g}$ is the gravity acceleration vector, P_α the pressure in phase and K_α is the phase permeability, which depends on the phase saturation S_α,

$$K_\alpha = k_{\mathrm{r}}\ (S_\alpha)\,\mathbf{K} \quad (11)$$

in which k_{r} is the relative permeability of phase and $\boldsymbol{K}$ is the absolute permeability, which is independent of the nature of the fluid. The sum of the saturation of the liquid and the gas phases should respect the following equation,

and the capillary pressure linking the fluid and liquid pressures is defined by:

$$S_l + \ S_g = 1, \quad 0 \leq S_\alpha \leq 1 \quad (12)$$

The constraint regarding the mass fraction of a component in a phase is,

$$\sum_{\kappa=H2O,H2} \chi_\alpha^\kappa = 1, \quad 0 \leq \chi_\alpha^\kappa \leq 1 \quad (14)$$

2.2 Temperature and pressure dependent viscosity and density

As water and H_2 migrate along the fault, their properties, such as density and viscosity, will change according to pressure and temperature. First, we will focus on the properties of the liquid saline water (i.e. brine) as well as gaseous H_2.

2.3 Liquid water density

As water density is a function of pressure (P) and temperature (T), its variation can become a main driving mechanism for water flow under the action of gravity in absence of over-pressurization. From experimental data fits, the volumetric mass variations of a reference water ρ_0 for temperature and pressure ranges of 0–1000°C and 0–500 MPa respectively, has been given by Linstrom and Mallard (2001), such as,

@ >p(- 2) * >p(- 2) * @

$$\rho_{l,mass}^{H2O}(P,\ T) = \rho_0 + (7.424 \times 10^{-7} \times \Delta P) + \ (-0.3922\ \times\ \Delta T\ ) + \left(-4.441\ \times\ 10^{-15} \times \Delta \mathrm{P}^2\right) + (4.547\ \times\ 10$$

& (15)

The evolution of a reference water volumetric mass $\rho_0 = 1004$ kg m^{-3}, depending on P and T, is shown in Figure 2, left. In the case of the presence of dissolved NaCl, the same equation can be used provided that the reference water volumetric mass takes into account the NaCl concentration at temperatures below 250°C. The evolution of the volumetric mass of a brine containing 26 wt% of NaCl, $\rho_0 \approx 1200$ kg m^{-3} (at 20°C and 1 atmosphere) is represented in Figure 2, right. Above 250°C, Equation 2 is not valid anymore and the evolution of the brine density needs to be formulated with major corrections (see Driesner et al., 2007).

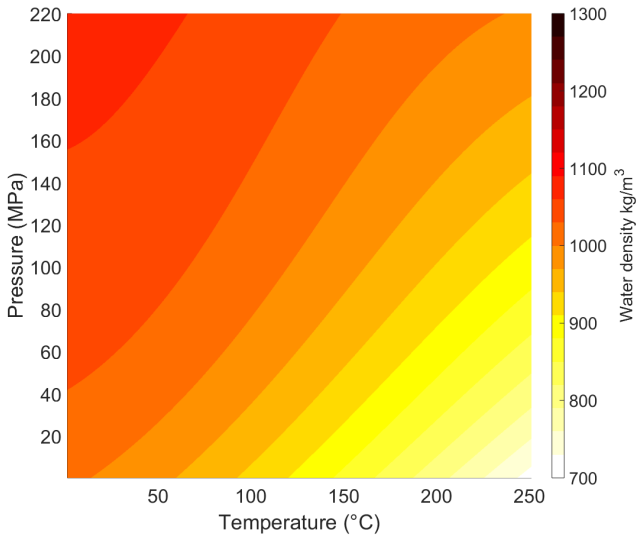

Figure 2. On the left, the pure water volumetric mass is represented as a function of pressure (P) and temper

2.4 Liquid water viscosity

Water viscosity is mainly temperature-dependent and follows the exponential decrease based on Rabinowicz et al. (1998) equation:

$$\mu_w(T) = 2.414 \times 10^{-5}\ \mathrm{e}^{\frac{570}{(T+133)}} \qquad (16)$$

As the concentration of NaCl increases, the evolution of the viscosity is modified. The most commonly used model to calculate the viscosity of H_2O-NaCl at elevated PT conditions is the one of Palliser & McKibbin (1998). However, Yu et al. (2017) proposed a revised empirical model that reproduces more accurately the experimental data by displaying smooth and expected extrapolation to PTx conditions at elevated temperatures and pressures, i.e. up to 1000°C and 500 MPa, and for salinities ranging from 0 to 100 wt% of NaCl. The viscosity at temperatures below 800°C is described by a ninth order polynomial as a function of temperature, such as,

$$\mu_{w-NaCl}\left(P,T,\chi_{\mathrm{NaCl}}\right) = \frac{\mu_w(P,T)(1+3\chi_{\mathrm{NaCl}})\left(\frac{800-T}{800}\right)^9}{\left(\frac{800-T}{800}\right)^9+\left(\frac{T}{800}\right)^9} + \frac{(\mu_w(P,T)(1+\chi_{\mathrm{NaCl}})+\mu^{800}_{\mathrm{NaCl}})\left(\frac{8T}{800}\right)^9}{\left(\frac{800-T}{800}\right)^9+\left(\frac{T}{800}\right)^9} \qquad (17)$$

Where χ_{NaCl} is the mass fraction of sodium chloride in the water, T is the temperature in °C, P is the pressure in bars and $\mu^{800}_{\mathrm{NaCl}}$ is a constant corresponding

to the viscosity of molten NaCl at 800°C (1500 $\text{Pa} \cdot \text{s}$).

In Figure 3, the viscosity of pure water is compared to the viscosity of a brine for which $\chi_{\text{NaCl}} = 26\%$ as functions of temperature.

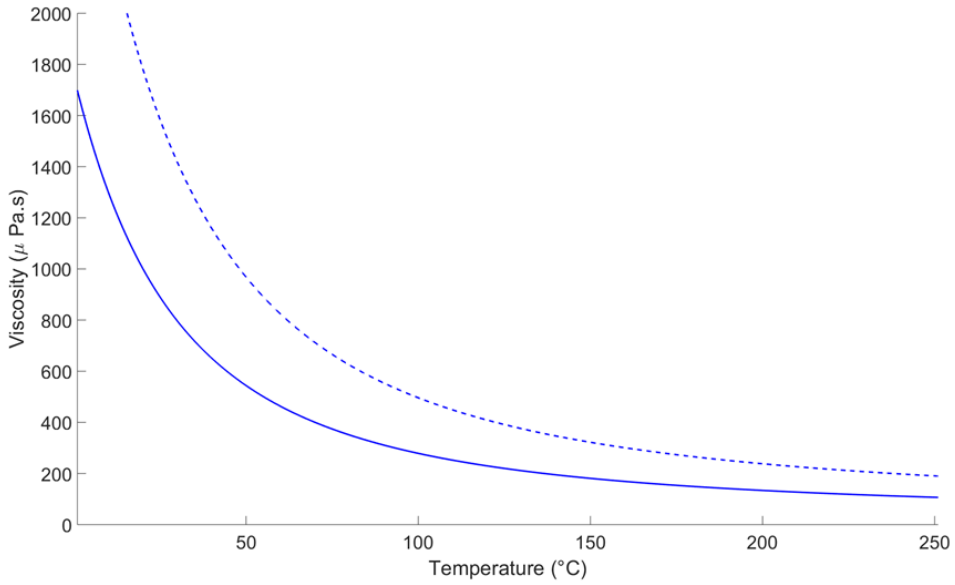

Figure 3. Viscosity comparison of pure water (solid blue curve) given by Equation 3 and brine (26 wt% NaCl

2.5 Dihydrogen gas density

The dihydrogen density depends on both pressure P and temperature T. We use the formulation proposed by Lemmon et al. (2008), such as,

$$\rho_{H_2}(P,T) = \frac{P_{H_2}}{\text{RT}} \left(1 + \sum_{i=1}^{9} a_i \left(\frac{100}{T}\right)^{b_i} \left(P_{H_2}\right)^{c_i}\right)^{-1} \quad (18)$$

Where P_{H_2} is the H_2 gas pressure expressed in MPa, T is the temperature expressed in Kelvin, R is the universal gas constant equals to 8.314 472 J mol^{-1} K^{-1} and the a_i, b_i and c_i coefficients are given in Table 3. The resulting effect of temperature and pressure on H_2 gas density is displayed in Figure 4.

Table 3. Constant associated with equation 17.

i	a_i	b_i	c_i
1	0.058 884 60	1.325	1.0
2	– 0.061 361 11	1.87	1.0

Table 3. Constant associated with equation 17.

3	– 0.002 650 473	2.5	2.0
4	0.002 731 125	2.8	2.0
5	0.001 802 374	2.938	2.42
6	– 0.001 150 707	3.14	2.63
7	$0.958\ 852\ 8 \times 10^{-4}$	3.37	3.0
8	$-0.110\ 904\ 0 \times 10^{-6}$	3.75	4.0
9	$0.126\ 440\ 3 \times 10^{-9}$	4.0	5.0

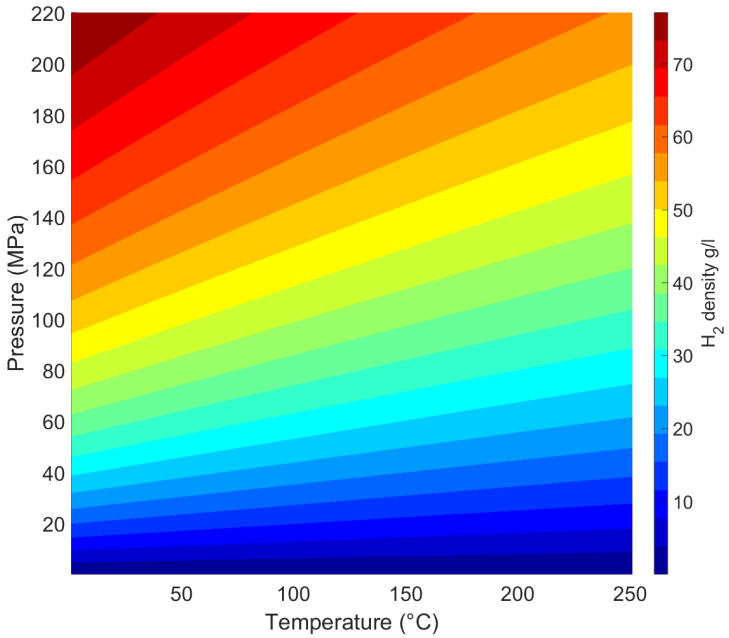

Figure 4. Effect of temperature and pressure on H_2 gas density

2.6 Dihydrogen gas viscosity

H_2 viscosity depends on both pressure P and temperature T. A wide-ranging correlation for H_2 viscosity has been developed by Muzny et al. (2013) using a symbolic regression methodology. As a consequence, we use their formulation in our model as their correlation covers the temperature and pressure ranges from the triple point (13.7 K, 7.2 MPa) up to 1000 K and 200 MPa (Figure 5).

Based on a differential evolution nonlinear fitting algorithm, the functional form of H_2 viscosity can be expressed as,

@ >p(- 2) * >p(- 2) * @ $_{H_2}\left(T, \rho_{H_2}(P,T)\right) =$ $_{0H_2}(T)+$ $_{1H_2}(T)\rho_{H_2}(P,T)+$

$$C_1 \quad {}_r{}^2 \times e^{\left(C_2 T_r + \frac{C_3}{T_r} + \frac{C_4 \rho_r{}^2}{C_5 + T_r} + C_6 \rho_r{}^6\right)} \quad \& \tag{19}$$

Where the scaled temperature is $T_r = \frac{T}{T_c}$ and the scaled density $\rho_r = \frac{\rho_{H_2}(P,T)}{\rho_{\mathrm{sc}}}$. As the temperature is expressed in Kelvin, the density $\rho_{H_2}(P,T)$ is in $\mathrm{kg} \cdot \mathrm{m}^{-3}$, and the viscosity μ is in $\mathrm{Pa} \cdot \mathrm{s}$. The quantity ρ_{sc} is a compressed-state density used for scaling that the symbolic regression procedure identified as *90.5* $kg \cdot m^{-3}$ whereas the critical temperature T_c = *33.145 K.*

The zero-density limit of the viscosity ${}_{0H_2}(T)$ is approximated by the following expression,

$$\overline{\underline{{}_{0H_2}(T) = \frac{0.021357(\mathrm{MT})^{0.5}}{\sigma^2 S^*(T^*)}}} \tag{20}$$

where $S^*$is a reduced effective cross section, M = *2.01588* is the molar mass of $\mathrm{H_2}$ in $\mathrm{g} \cdot \mathrm{mol}^{-1}$, is a length scaling parameter in nm, and the temperature T is in K. The effective cross section has a functional form, such as

$$@ >\mathrm{p}(\text{- } 2) * \ >\mathrm{p}(\text{- } 2) * @ \ln\left(S^*\left(T^*\right)\right) = \sum_{i=0}^{4} a_i \left(\ln\left(S^*\left(T^*\right)\right)\right)^i \quad \& \tag{21}$$

The reduced temperature is $T^* = k_B T/$ and $/k_B$ is an energy scaling parameter in K. For the scaling parameters and */kB,* = *0.297* nm and $/k_B$ = *30.41 K.*

The initial-density coefficient of the viscosity ${}_{1H_2}(T)$ may be written such as,

$$\overline{\underline{{}_{1H_2}(T) = B_\mu(T) \quad {}_{0H_2}(T)}} \tag{22}$$

where $B_\mu(T)$ is the second viscosity virial coefficient and ${}_{0H_2}(T)$ is the zero-density contribution. $B_\mu(T)$ can be expressed such as,

$$\overline{\underline{B_\mu(T) = \frac{B_\mu^*(T^*)}{\sigma^3}}} \tag{23}$$

With

$$B^*_\mu\left(T^*\right) = \sum_{i=0}^{6} b_i \left(T^*\right)^{-1} \qquad (24)$$

where T^*, are as defined earlier.

The coefficients of Equations 19, 21 and 24 are presented in Table 4. The evolution if H_2 viscosity is represented in Figure 5.

Table 4. Constant associated with equations 19, 21 and 24.

i	a_i	b_i	c_i
0	2.09630×10^{-1}	-0.1870	-
1	-4.55274×10^{-1}	2.4871	6.43449673
2	1.43602×10^{-1}	3.7151	$4.56334068 \times$
3	-3.35325×10^{-2}	-11.0972	$2.32797868 \times$
4	2.76981×10^{-3}	9.0965	$9.58326120 \times$
5	-	-3.8292	$1.27941189 \times$
6	-	0.5166	$3.63576595 \times$

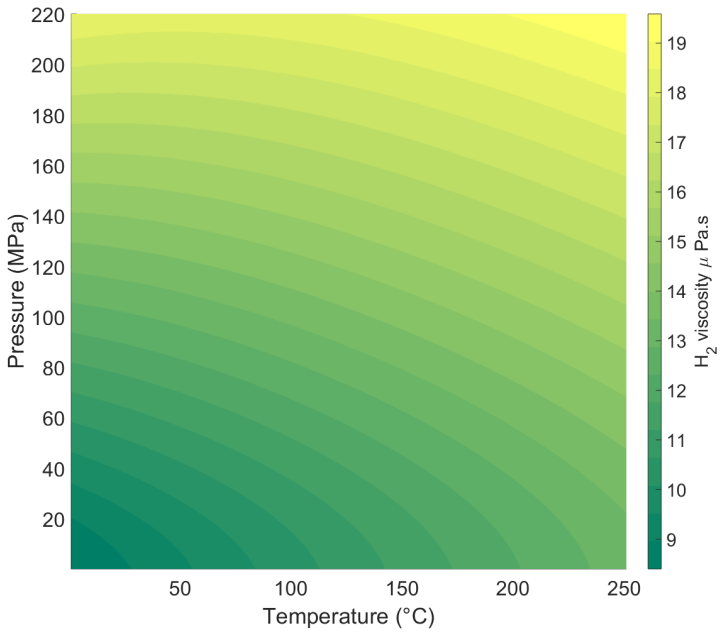

Figure 5. Effect of temperature and pressure on H_2 gas viscosity according to Equation 19.

2.7. Dihydrogen solubility in Water

According to Eq. 12, the sum of the saturation of the liquid and the gas phases should be equal to 1. Thus, it is necessary to assess the solubility of H_2 in water. Indeed, serpentinization occurs when ultramafic rocks originating from a mantle body (e.g. peridotites) encounter water. Serpentinized rocks undergo major changes in pressure and temperature conditions, causing them to react in presence of water and produce fracturing within the progression front of the chemical reaction (Zhang et al., 2019). As serpentinization processes eventually lead to the clogging of the rock pore space, expelled fluids migrate until they are channeled through major draining paths along faults. Temperature and pressure conditions change over long distances up to the surface, and impact the amount of gas dissolved in water. Therefore, knowledge of the phase equilibria regarding the solubility of H_2 in water along the fault is necessary to study the quantity of H_2 that can be transported in water. Based on experimental measurements, a simple formulation for quick and accurate calculations of H_2 solubility in water has been proposed by Chabab et al. (2020). Using the mole number of H_2 (n_{H_2}) and H_2O (n_{H_2O}), the solubility of H_2 in water is determined by,

$$\chi^0_{H_2} = \frac{n_{H_2}}{n_{H_2}+n_{H_2O}} \quad (27)$$

The solubility in terms of mole fraction χ_{H_2} can be converted in terms of molality m_{H_2} (in mol.kg^{-1}) by the following relationship:

$$m_{H_2} = \frac{100\ \chi^0_{H_2}}{M_{H_2O}\left(1-\chi^0_{H_2}\right)} \quad (28)$$

The solubility data of H_2 in water have been correlated by the following equation (Chabab et al., 2020):

$$\chi^0_{H_2} = b_1 PT + \frac{b_2}{T}T + b_3 P + b_4 P^2 \quad (29)$$

where the temperature T is in K and the pressure P is in bar and with parameter values given in Table 5.

Table 5. Parameter values of Equation 29.

b_1	b_2	b_3	b_4
3.338844x10^{-7}	0.0363161	-0.00020734	-2.1301815x10^{-9}

The fitting range of pressure and temperature values to establish Equation 14 for H_2 solubility in pure water is $273.15 < T$ (K) < 373.15 and $1 < P$ (bar) < 203. Indeed, the parameter values b_1 to b_4 were established based on experimental data up to 200 bars. In our model, we have extended the scope of Equation 14 to higher pressures (up to 1 kbar) and temperatures (up to 250°C or 523.15 K), as the H_2 solubility data provided by Seward and Franck (1981) can be well predicted while keeping the same coefficient values (Figure 6, left).

Note that to calculate the solubility of H_2 in brine, a simple correlation taking into account the effect of temperature, pressure and NaCl molality has been developed by Chabab et al. (2020). The proposed correlation is based on a Setschenow-type relationship, and is defined by:

$$\ln\left(\frac{\chi_{H_2}^{\text{brine}}}{\chi_{H_2}^{0}}\right) = a_1 m_{\text{NaCl}}^2 + a_2 m_{\text{NaCl}} \quad (30)$$

with the constant values given in Table 6.

Table 6. Constant associated with equation 30.

a_1	a_2
0.018519	-0.30185103

Knowing the solubility $\chi_{H_2}^{0}$ of H_2 in pure water at the system temperature and pressure, the solubility $\chi_{H_2}^{\text{brine}}$ of H_2 in brine at a given molality m_{NaCl} is obtained by Equation 13 and presented in Figure 6 right.

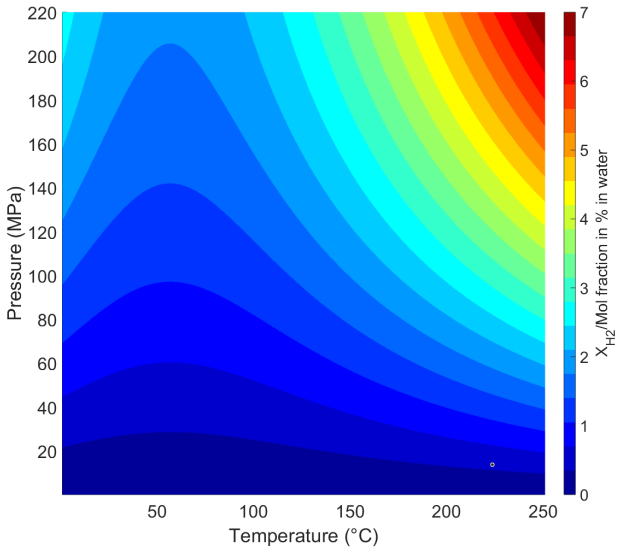

Figure 6. Effect of temperature and pressure on H_2 solubility in pure water (left) and in brine with a NaCl co

2.8. Capillary pressure

Yekta et al. (2018) have performed core-flooding experiments to measure capillary pressure, i.e. the pressure difference across the interface between two phases, for the H_2–water system in a porous sandstone. A capillary pressure dataset has been obtained from semi-dynamic capillary pressure and mercury injection capillary pressure measurements. Combining the two types of data allows the determination of the capillary pressure evolution for the H_2–water system over the entire water saturation range,

$$P_c\left(S_l\right) = P_d\left(S_w\right)^{\frac{-1}{\lambda}} \quad (31)$$

Where $\lambda = 0.725$ is the Brooks-Corey parameter and $P_d = 5.0\ kPa$ is the entry pressure. The Brooks-Corey capillary pressure formulated in Equation 31 is plotted in Figure 7.

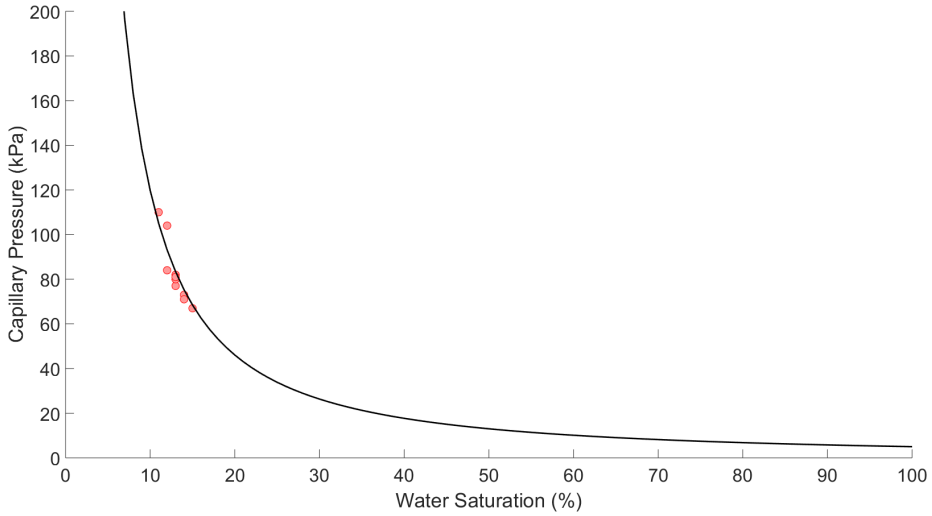

Figure 7. Calculation of hydrogen capillary pressure (black solid curve) from experiments represented by red

2.9. Permeability along the fault zone

Permeability within the damage zone along a fault plane is strongly dependent on the in-situ effective stress. For low effective stress, connected fractures are open and exhibit an overall maximum permeability value. As the effective stress increases, fractures tend to close and water can be channeled as long as the rock asperities due to roughness, withstand the total stress loading. Thus, the permeability drops dramatically when these bridges collapse and only connected micro-cracks can still overcome the intrinsic permeability due to the porosity of the medium.

The complex evolution of permeability within the damage zone can be expressed using a "Two-Part Hooke's Model" (Zheng et al., 2015). In this formulation, the permeability is the sum of two terms describing 1) the soft-behavior of the fracture set, responsible for the significant permeability reduction observed for low effective stress levels, and 2) the hard-behavior that involves the bulk volume of the rock body, when closure of the connected draining zones occurs. Based on this concept, Donzé et al. (2020a) proposed a stress-dependent permeability $k_w\left(\sigma_{\text{eff}}\right)$ such as,

$$k_w\left(\sigma_{\text{eff}}\right) = k_s\left(\sigma_{\text{eff}}\right) + k_h\left(\sigma_{\text{eff}}\right) \quad (32)$$

Where $k_s\left(\sigma_{\text{eff}}\right)$ is related to the soft-behavior expressing the evolution of the permeability for low effective stress values and $k_h\left(\sigma_{\text{eff}}\right)$ is related to the hard-behavior, which provides the permeability for high effective stress values.

For low values of the effective stress, $k_s\,(\sigma_{\text{eff}})$ can be expressed as,

$$k_s = k_0 \left(\gamma e^{-c_{f0}\ \Delta}\ \right)^m \quad (33)$$

Where k_0 is the permeability at the reference stress $_{\ 0}$, $\Delta\sigma = \sigma_{\text{eff}} - \sigma_0$ is the differential stress between the effective stress and the reference stress, c_{f0} is the compliance of the fracture at the reference stress $_{\ 0}$, is the stress sensitivity coefficient and an exponent m (see Donzé et al., 2020a for details). When m = 3, the permeability evolution corresponds to the classical cubic law, which does not represent the sharp transition of the permeability of low permeable medium observed when the effective stress tends to zero.

As a consequence, the value of k_s becomes negligible for $\Delta\sigma\ \gg \frac{1}{c_{f0}}$ and the hard-behavior term k_h, becomes the first order component of the global permeability such as,

$$k_h = k_0 e^{[-3C_f \Delta\sigma]} \quad (34)$$

With the compliance C_f now depending on the effective stress, such that,

$$C_f = \frac{c_{f0}}{\alpha\Delta\sigma}\left(1 - e^{-\alpha\Delta\sigma}\right) \quad (35)$$

Where α is the declining rate of fracture set compressibility as the effective stress increases.

Varying parameter values enables the coverage of different ranges of permeability values for the fault zone. We consider the permeability bounded between 10^{-16} m^2 and 10^{-17} m^2 that represents the limit between two flow regimes as over-pressurization is the main driving effect for fluid flow above 10^{-17} m^2, and natural convective flow can appear easily in case of a favorable temperature gradient below 10^{-16} m^2 (Rowland & Sibson, 2004). From these considerations, we consider two different evolutions for our permeability model, such as,

- a low-permeability fault in shale, calibrated from experimental water injection tests in Tournemire underground laboratory (Donzé et al., 2020a) with a residual permeability around $k_{w\_residual\_low} = 10^{-20}$ m^2 for high effective stress values,
- a high-permeability fault, using the same parameter values but with a residual permeability around $k_{w\_residual\_high} = 10^{-13}$ m^2. This value falls in the range of values for which thermal buoyancy-driven flow can occur in a fault zone.

The evolutions of these two permeabilities are represented in Figure 8.

2.10. Relative permeability along the fault zone for dihydrogen gas

Several factors can affect the permeability of gaseous H_2 along the fault zone. In case of dry flow, i.e. absence of water, the permeability corresponds to the absolute permeability of the medium (for sandstone see Yekta et al., 2018). In some clayrocks, chemical reactions with high kinetics can decrease dramatically the permeability (Ghanizadeh et al., 2014; Duan et al., 2014). Gas transport in poorly permeable rocks can be also affected by slip flow (Klinkenberg effect), resulting in deviations from Darcy's law (Ghanizadeh et al., 2014). Slip flow occurs when the mean free path of the gas molecules approaches the average diameter of pore aperture in porous media, causing the velocity of individual gas molecules to accelerate (slip) when contacting pore walls. Under slip flow conditions, the measured (apparent) permeability to gas $k_{app\_H_2}$ is a function of mean pore pressure (Klinkenberg, 1941), such as,

$$k_{app\_H_2} = k_{\infty}\left(1 + \frac{b_k}{P_f}\right) \quad (36)$$

where (k_{∞}) is the intrinsic permeability value as a function of the H_2 mean pressure (P_f) and coefficient b_k known as the Klinkenberg slip factor or the Klinkenberg coefficient. Based on the Klinkenberg phenomenon, the apparent gas permeability coefficients k_{gas} approaches a limiting value at infinite mean pore pressure. This limiting permeability value is commonly referred to as the Klinkenberg-corrected permeability (k_{∞}). Gas slippage phenomenon typically occurs in the laboratories when gas flow experiments are conducted at low pressures (Florence et al., 2007). Increasing gas pressure during tests reduces gas slippage effect while decreasing the effective stress, which in turn influences the permeability. The coupled effect of gas slippage and effective stress on shale permeability remains unclear (Yang et al., 2017), and as a first approximation we will neglect the contribution of gas slippage, i.e. $k_{H_2} = k_{app\_H_2}$.

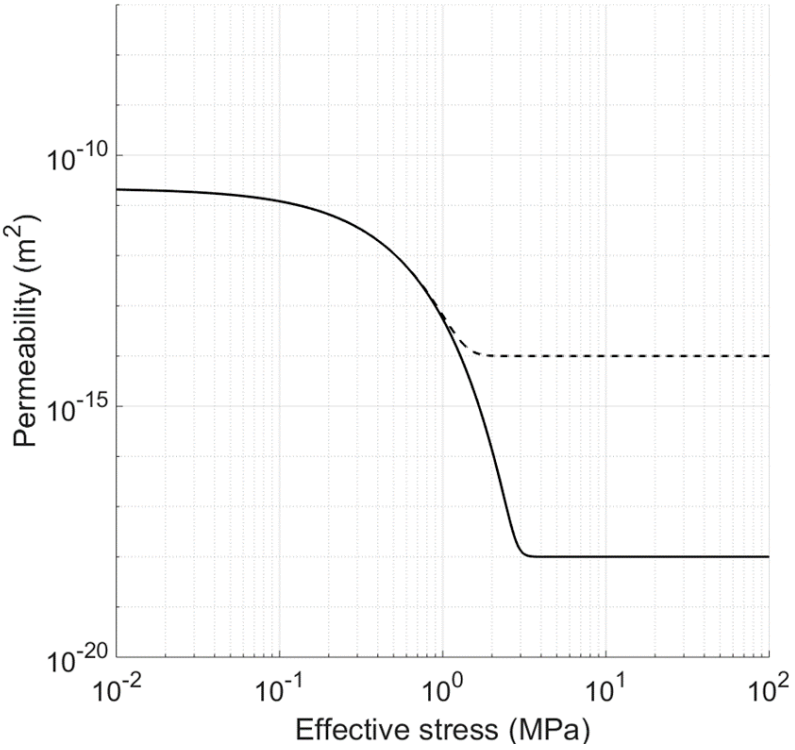

Figure 8. Permeability evolution along the fault depending on the effective stress. The dashed curve correspo

Water saturation (S_w) is another important influencing factor on H_2 gas flow in porous media (Pan et al., 2021). Water saturation in shale gas reservoirs ranges from 15 to 35% (Peng, 2021). The apparent permeability can be modified using the relative permeability ratio $k_{r\_H_2}$, such as, $K_{H_2} = k_{H_2} \times k_{r\_H_2}$. It is well-established that $k_{r\_H_2}$ is a function of S_w and rock wettability. However, available data is very scarce for H_2 and water: only one dataset exists to our knowledge where $k_{r\_H_2}$ and the associated water relative permeability ratio k_{r_w} were measured at in-situ reservoir conditions (Yekta et al., 2018; Figure 9). These results indicate a very poor ability for H_2 to flow through saturated medium. The Yekta et al. (2018) data set has been fitted using an exponential function such as,

$$k_{r\_H_2} = e^{-0.12(Sw-10)} \quad (37)$$

Note that this equation is verified for water saturation levels varying from 13% to 90% only.

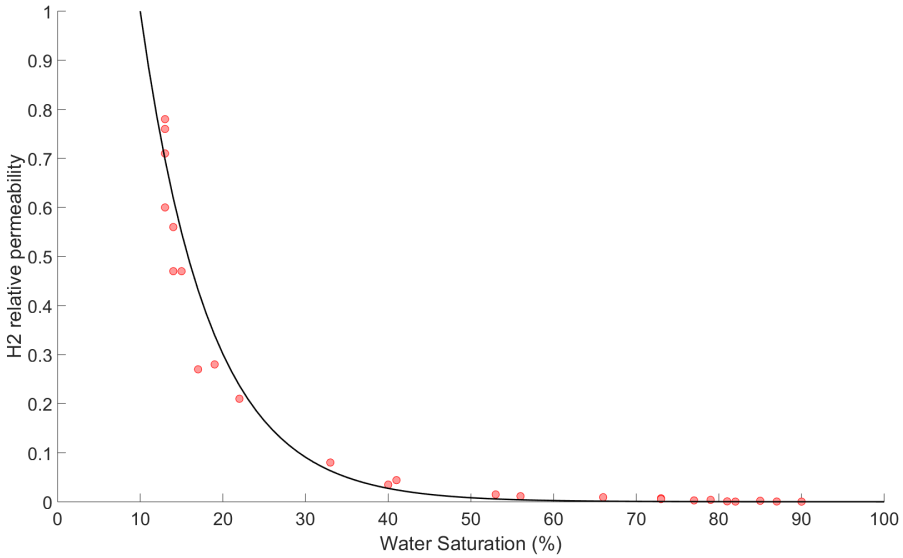

Figure 9. Calculation of H_2 relative permeability from capillary pressure experiments. The relative permeabil

3. Numerical model methodology and results

We first investigate independently H_2O (liquid) and H_2 (gas) flows using the geothermal module of MRST (Collignon et al., 2020). The system of coupled nonlinear partial differential equations describing the conservation of mass and energy (Equations 1-9) is solved using a finite volume method (Lie, 2019). A Newton's method is used, in which the Jacobians are computed by automatic differentiation. The equations of state to account for density and viscosity changes (Equations 15-24) have been plugged in the geothermal module, as well as the permeability and relative-permeability (Equations 32-37). We account indirectly for mechanical deformation in our model regarding the permeabilities and porosity, which depend on the effective stress values. Geochemical processes, such as water-rock interactions are neglected.

3.1 Hydrothermal convection results from 2D water models

In order to verify the correct formulation of the MRST model for our study purposes, we first simulate a hydrothermal convection of water (i.e. $= H_2O$) to compare with the results obtained by Guillou-Frottier et al. (2020). We also restrict our study to the (P,T) domain in which fluid stays in a liquid phase (no vapor phase, i.e. $\alpha = l$ only). A 1.5 km-thick and 4.5 km-wide permeable medium is thermally insulated on both vertical sides. Fixed temperature conditions of 0 and 400°C are imposed on the top and bottom boundaries, respectively. A no-flow condition is imposed on all boundaries except for the top

one, which is set up at a pressure of 10^5 Pa (Figure 10). As already shown by some studies (e.g., Rabinowicz et al., 1998), the intensity of thermal convection (i.e. number of upwellings or maximum fluid velocity value) increases with permeability. Convective wavelength decreases with permeability, and several internal upwellings are obtained in the case of high permeability. For reference, the resulting pattern of convection for a permeability of 10^{-13} m^2 obtained with MRST is presented in Figure 10.

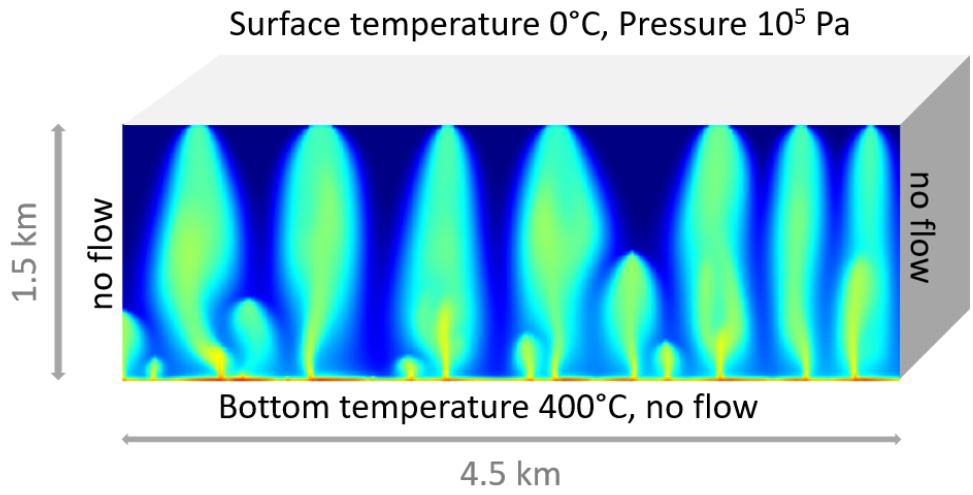

Figure 10. Hydrothermal convection with a high number of upwellings observed for a permeability at 10^{-13} m

In the shallow crust (i.e. 10-15 km, above the brittle–ductile transition), permeability is expected to decrease with increasing lithostatic pressure (e.g., Achtziger-Zupančič et al., 2017). In the case of a constant-pressure boundary condition at the top surface, the decrease of permeability K can be considered as a first approximation as an exponential function of depth such as (Guillou-Frotier et al., 2020),

$$K = 5.10^{-15}\ e^{-\frac{z}{\vartheta}} \quad (38)$$

Where z is the depth position and is a chosen coefficient adjusting the vertical evolution of the permeability.

The consideration of a depth permeability dependence modifies dramatically the convective patterns (Figure 11). The results of numerical simulations carried out either by Comsol Multiphysics™ software (Guillou-Frotier et al., 2020) or by MRST (this work) exhibit quantitatively similar trends and indicate that the

generated number of upwellings decreases as the evolution of the permeability is controlled by the coefficient (cases a, b, c, and d of Figure 11). Note that the decrease in the number of upwellings can be explained by the asymmetric distribution of temperature and permeability: cold fluids are located in the most permeable zones, whereas hot fluids encounter less-permeable media at depth. Consequently, cold downwellings are favored and a general cooling is obtained in case d (Guillou-Frotier et al., 2020).

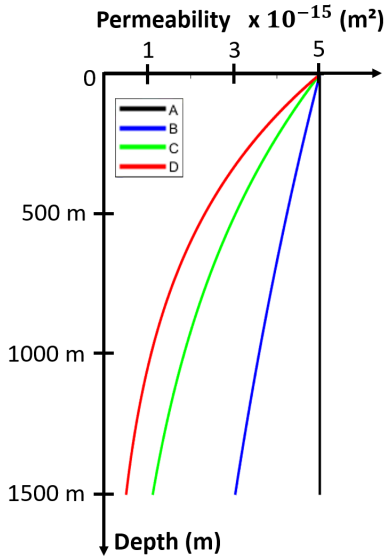

Figure 11. On the left, representation of the permeability dependence to depth for different coefficients values

3.2 H_2 pulsing system through the caprock

After having successfully verified the ability of our MRST model to reproduce quantitatively complex flows associated to hydrothermal convection, we propose a configuration at depth to eventually generate cyclic bursts of H_2 at the surface. For this purpose, we set up a numerical model representing a permeable planar fault capped by an impermeable layer and impose a constant incoming source of H_2 gas at its basement. We carried out a parametric study to assess how different parameters, such as thickness, depth position, permeability contrasts for the low permeability layer and H_2 flow rate can control the pulsing flow regime of H_2 at the surface. First, we define a reference case for which cyclic pulses of H_2 are generated. Second, based on this configuration, we assess the respective roles of the previously cited parameters on H_2 flow. From these results, we propose a range of values for the initial in-situ effective stress at the basement of the impermeable layer and the incoming H_2 flow rate, which are

required to generate a sustainable pulsing regime of H_2 at the surface. Then, we test this model to predict other configurations using different values of the listed parameters, and also enable the modification of the tectonic regime, i.e. a different ratio between the vertical and horizontal stresses to ensure that the H_2 pulsing regime observed at the surface is still predicted by our permeability-effective stress model.

3.2.1 Reference case

The reference configuration is a 1000 m-deep vertical fault (Figure 12, left) with a temperature gradient of 30°C/km, based on the one observed in the Mauléon basin located in the Western part of the Pyrenees (Bonté et al., 2010). As a first approximation, the in-situ hydrostatic configuration is approximated through Eq. 39 that provides a solubility value $\chi^0_{H_2}$ for H_2 in pure water lower than 0.25% at a 1000 m depth (and even lower in brine), leading us to focus only on the gas form of H_2 (i.e. $= H_2$ and $\alpha = g$ only) and neglecting the coupling with H_2O. We emphasize here, that this approximation is only valid for low-solubility gases like H_2, CH_4 or He, but cannot be applied to highly soluble gases like CO_2 or H_2S. The fault draining zones are set to a high residual permeability value of 10^{-14} m^2 (red curve in Figure 12, right), with an imposed incoming flux of H_2 of 10^5 mol/day at their bottoms (Figure 12, left) based on a value estimated by Cannat et al., (2010).

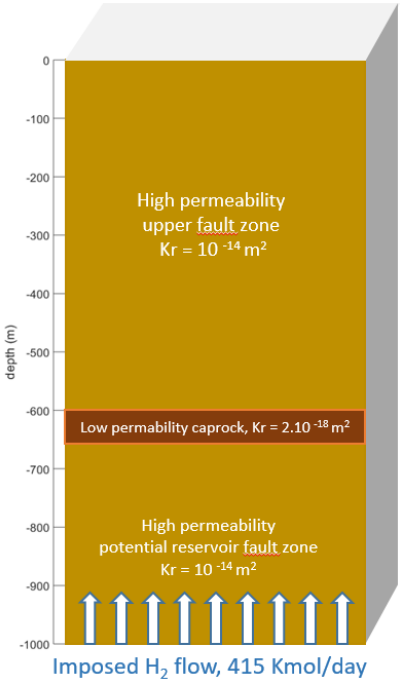

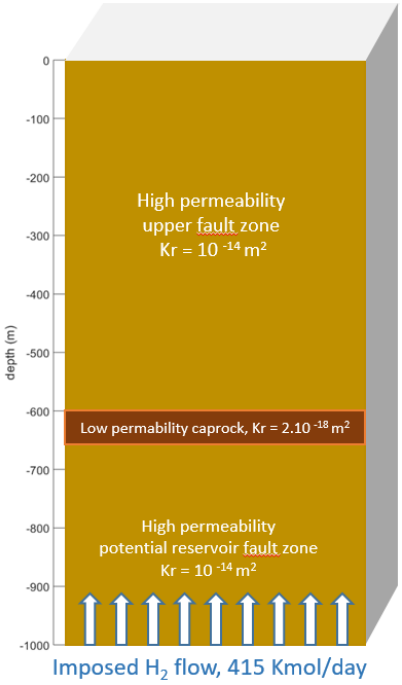

Figure 12. On the left, the geometry of the modeled vertical fault with an imposed basal flow of H_2, whose u

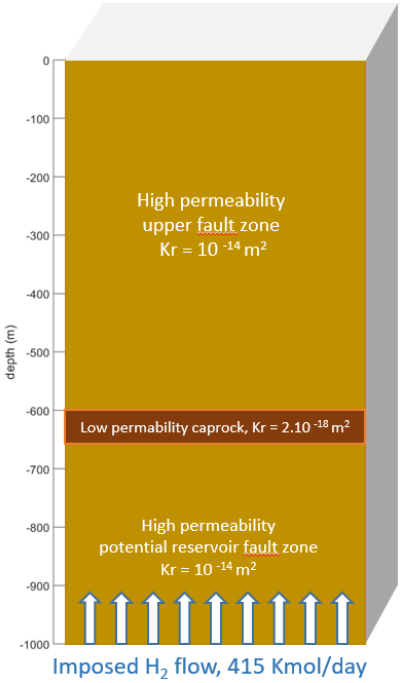

The low permeable layer is located between depths of -650 m and -600 m, i.e. with a thickness of ~50 m and a residual permeability of ~2.10^{-18} m^2 (Figure 12, right), which can be obtained using Eq. 32 for a given level of water saturation in presence of e.g. an aquifer or a low permeable rock like clay. Both permeabilities depend on the in-situ effective stress and their formulations are based on Equations 32-35. In this parametric study, we consider two other permeability values (2.10^{-19} m^2 and 2.10^{-17} m^2) for the low residual permeability (blue dots and dash lines respectively in Figure 12, right) that allow the comparison of low and high permeability layers and the assessment of the contribution of the relative permeability in H_2 flow regime. The fluid pressure and the in-situ total stress normal to the fault plane σ_h control the effective stress. In this reference configuration, this total stress value is given for an extensive tectonic regime, with $\sigma_h = 0.6 \ _V$, where σ_V is the vertical stress generated by the overburden rock and calculated for a rock volumetric mass of 2700 kg/m^3. In the permeability formulation (equations 33-35), $\sigma_0 = \sigma_h$. Figure 13 presents the results of the simulation of the evolution of H_2 flow at the surface using the reference model as function of time (Figure 13, top), the evolution of permeability at the bottom of the low-permeability layer (Figure 13, middle) and the evolution of effective stress at the same depth (Figure 13, bottom). This configuration allows the generation of pulsing fluxes of H_2 at the surface (Figure 13, top) that exhibit a time delay of Δt compared to the moment of promt stress release and permeability decrease of the impermeable layer. This delay corresponds to the time

needed for H_2 to reach the surface after crossing both the impermeable layer and the upper high-permeability zone of the fault. This permeability decrease also corresponds to a new increase of the effective stress inside the impermeable layer, i.e. the closure of this layer after an H_2 burst sequence. The fluid pressure below the caprock decreases abruptly before increasing again until the next pulsing sequence.

The two main steps of a pulsing sequence can be visualized across the entire depth of the fault (Figure 14). The "A" profile (Figure 14, top) is a snapshot of a simulation (point A, Figure 13) when the effective stress is at its minimum value whereas the permeability is at its maximum at the top of the low-permeability layer: H_2 has crossed the low-permeability zone and migrates towards the surface as from the previous pulsing sequence its flow at the surface is still minimum (Figure 13, top) and the bottom of the low permeable layer is already closing (Figure 14, A-left). The "B" profile (Figure 14, bottom) represents the closed state of the low permeable layer, i.e. the lowest permeability value reached during the pulsing sequences corresponding to the maximum effective stress value, and, considering the time delay Δt, to the maximum flow rate of H_2 appearing at the surface (Figure 13, top).

The required time for H_2 gas to refill the lower part of the zone to reach again the critical pressure to "reopen" the fault is about 90-100 days (Figure 13 top). This periodic process is sustainable and the fault behaves as a fault-valve system generating bursts of H_2 at the surface with variable maximum flow values ranging from 4.5×10^5 to 8×10^5 moles/day.

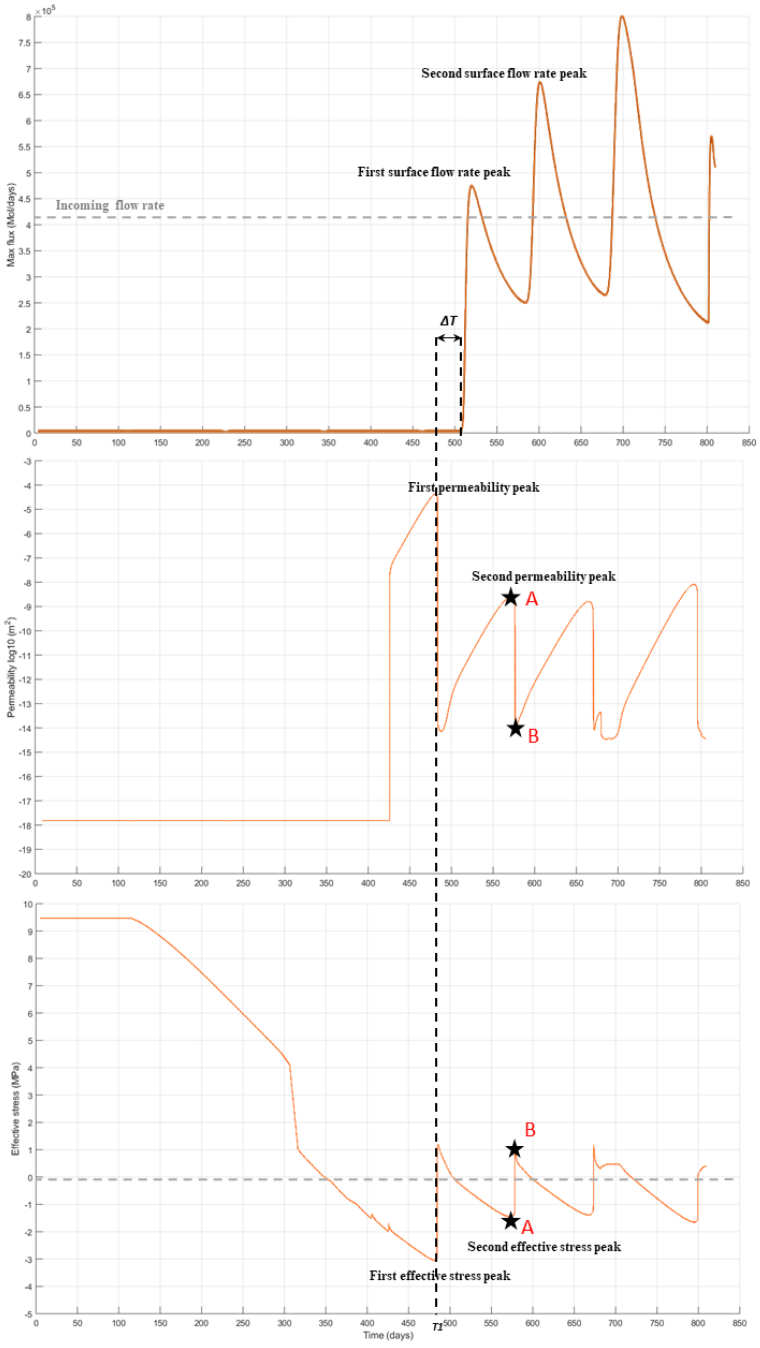

Figure 13. Results of the numerical simulation of the reference case. On the top, the time evolution of the H_2

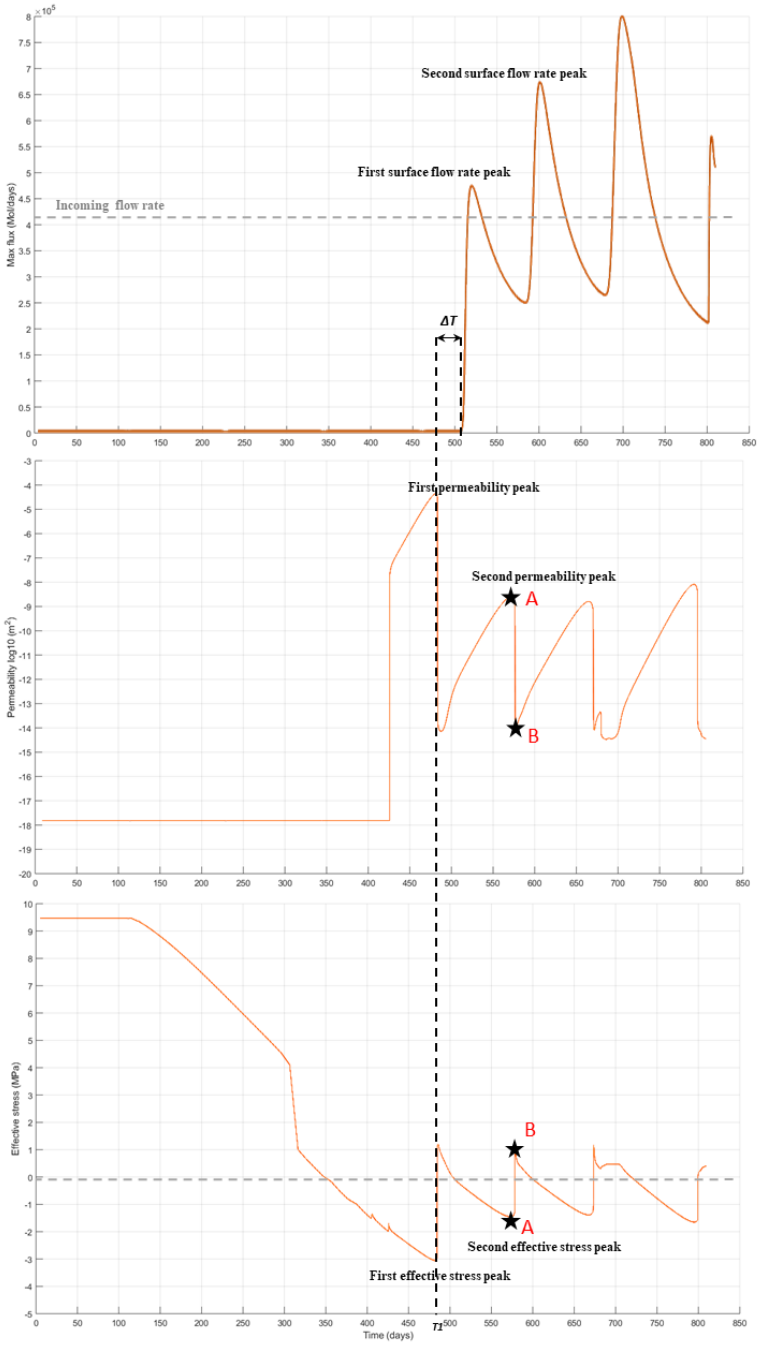
Second surface flow rate peak
First surface flow rate peak
Incoming flow rate
ΔT
Max flux (Mol/days)
First permeability peak
Second permeability peak
A
B
Permeability log10 (m²)
B
A
Second effective stress peak
First effective stress peak
Effective stress (MPa)
Time (days)
T1

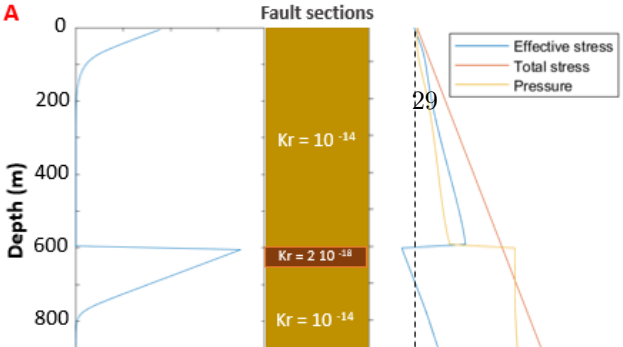
A
Fault sections
Depth (m)
Kr = 10 -14
Kr = 2 10 -18
Kr = 10 -14
Effective stress
Total stress
Pressure

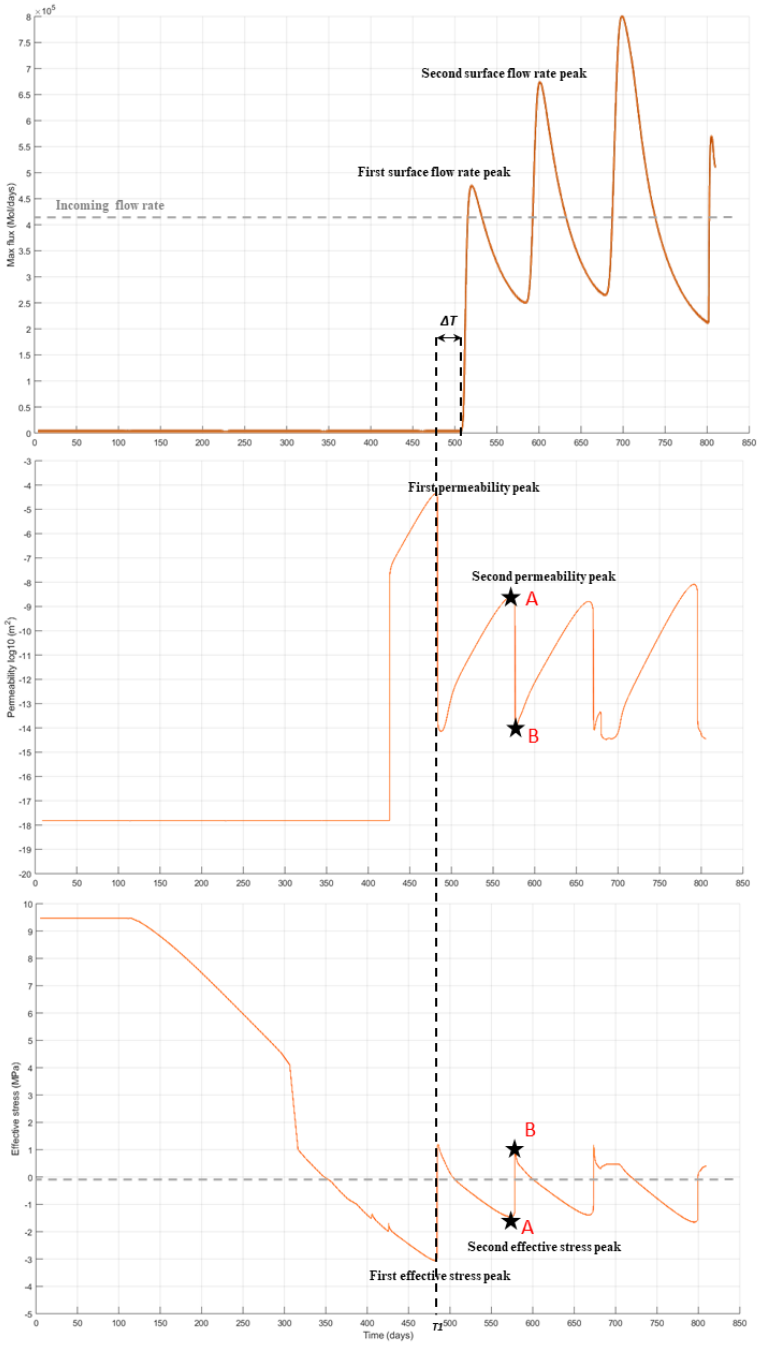

Figure 14. At the top left, the permeability vertical profiles and at the top-right, the associated profiles of H_2

3.2.2 Contribution of the input H_2 flow rate

The pulsing emissions at the surface is thus controlled by the ability of the low-permeability layer to open and close periodically. To account for varying incoming flow rates, we consider a reference flow rate of 4.10^5 moles/day bounded by a maximum flow rate (8.10^5 moles/day) and a minimum one of 2.10^5 moles/day (Figure 15). Compared to the reference case (brown curve b), imposing a double flow rate (green curve j) does not produce a sustainable pulsing system. After two brief pulses spaced by ~50 days, the emitted flow rate at the surface becomes constant, with a flow rate equals to the basal incoming flow rate, presenting now a steady-state regime. The low-impermeability layer dramatically opens up to 10^{-3} m^2 due to the large fluid pressure, and then remains hydraulically open because the fluid pressure at the bottom part of the fault does not decrease enough to allow its closure. Indeed, this phenomenon generates an effective stress close to 1 MPa, inducing inside the low-permeability zone a permeability equals to the higher ones. Therefore, the fluid crosses the entire fault with a constant permeability of about 10^{-14} m^2. At the opposite, imposing low incoming flow rate value for H_2 leads to a clear sustainable pulsing system with high flow rate amplitudes at the surface (black curve (i) in Figure 15). The longer time needed to refill the bottom part of the fault at a sufficiently high pressure induces a slower decrease of the effective stress inside the low-permeability zone, down to -3 MPa (i.e. a fluid pressure higher than the minimum in-situ stress), leading to a smaller maximum aperture of the fault (10^{-6} m^2) before closing again. With this smaller opening, the maximum surface H_2 flow rate is indeed lower and varies from 5×10^5 to 5.5×10^5 moles/day (Figure 15, black curve). Thus, an increased H_2 flow rate modifies the pulse amplitudes but also their periodicity that increases accordingly from a reference period of 90-100 days to ~250 days.

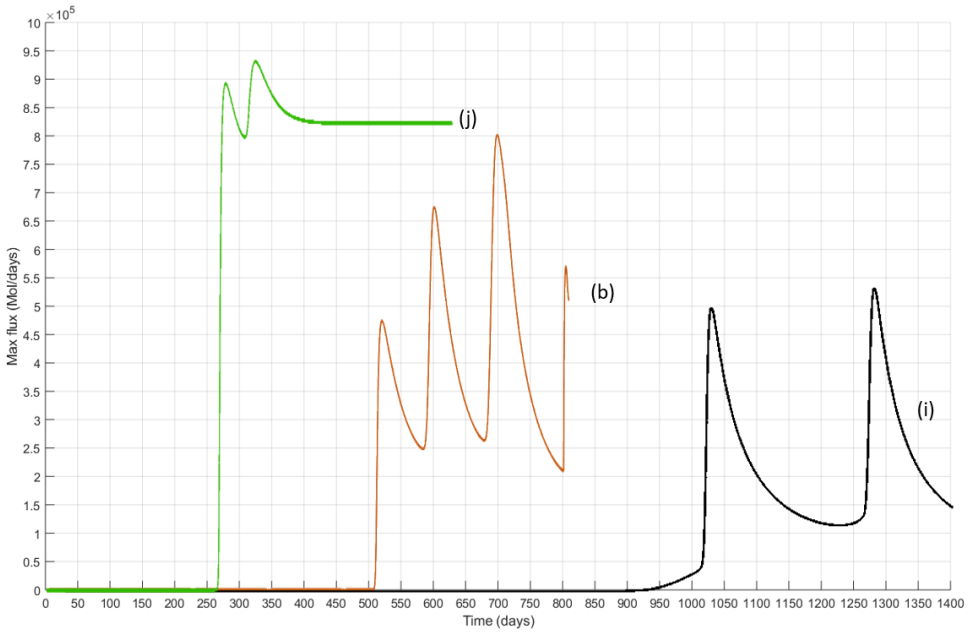

Figure 15. Resulting H_2 flow rates at the surface for three different values of H_2 incoming flow rate at the bot

3.2.3 Contribution of the depth of the low permeable layer

While considering the reference configuration, we modify the depth of the low permeable layer from -650 m to -750 m, -550 m and -350 m (Figure 16, bottom) and plot the evolution of simulated surface H_2 flow rates (Figure 16, top-left). In order to compare their respective periodicities, we superimpose the resulting curves to the reference case curve (brown curve b; Figure 16, top right). For the two cases with the deepest low-permeability layer (i.e. -650 m (b) and -750 m (blue curve 'a')), the pulsing response is clearly visible and yield similar periodicities (90-100 days). As the depth decreases, three observations can be made: (I) the first burst of H_2 flow rate increases sharply (-550m; green curve 'c') before disappearing (-350m; purple curve 'd'), (II) a pseudo-periodicity is observed for -550m ('c') with a longer time range of ~170 days, and (III) a continuous flow equals to the incoming flow rate at depth for the shallow case (-350m; 'd'). As the depth of the low-permeability layer decreases, the size of the fault lower part increases, leading to higher fluid pressure penetrating the low permeable zone. The sharp increase of effective stress-dependent permeability induces a large flow of H_2 propagating along the fault to the surface.

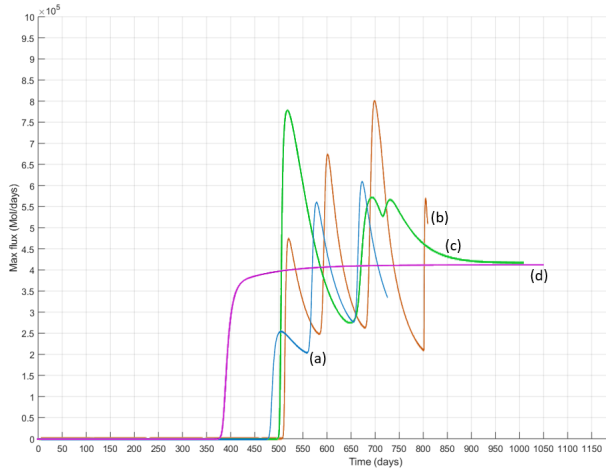

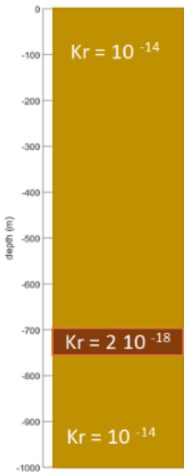

(a)

Figure 16. Bottom: four different depths for the impermeable layer are considered, -750 m (case 'a'), -650 m (

On the other hand, the effective stress tends to zero for a depth shallower than -200 m (Figure 14) inducing a dramatic increase of permeability that cannot slow down H_2 migration towards the surface anymore. Thus, no pulsing system can be generated with a shallow low-permeability layer (> -200 m) using the permeability-effective stress relationship given by equations 32-37. This means that the initial insitu effective stress state inside the low-permeability layer must be high enough (> 8 MPa for the present model) to remain in the low range of permeability values to potentially generate a pulsing system.

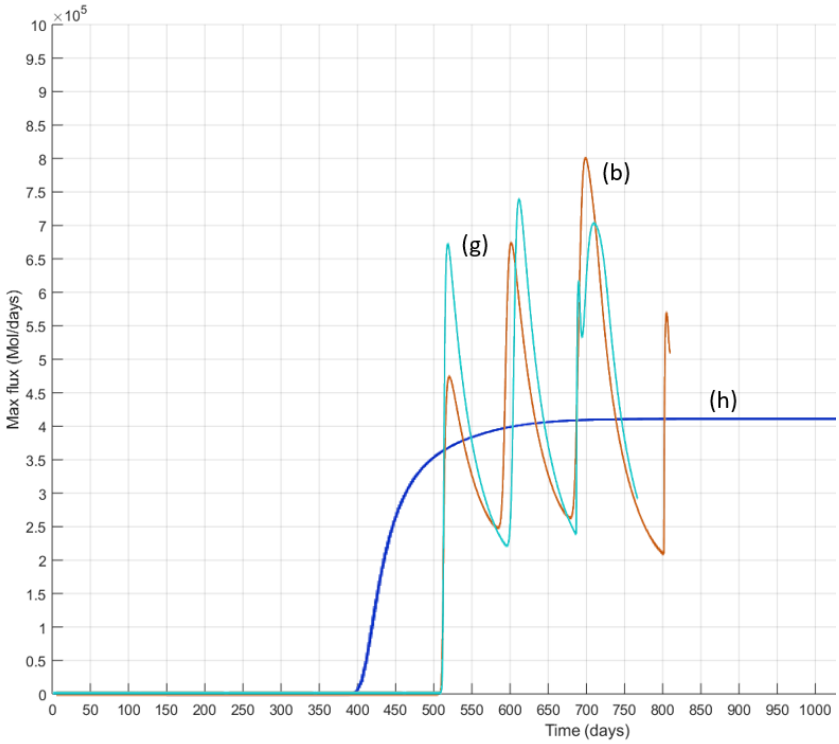

Figure 17. Resulting flow rates at the surface for three different permeability values of the low-permeability la

3.2.4 Contribution of the residual permeability of the low-permeability layer

The previous results lead to question the respective roles of the residual permeability versus the effective stress state in the low-permeability layer. Compared to the reference case, dividing the residual permeability of the low permeable zone by ten (10^{-19} m^2 rather than 10^{-18} m^2) results in a sharper pulsing signal at the surface while expressing the same periodicity and a more constant surface flux pattern regarding pulse amplitude (Figure 17, curve 'g'). In contrast, when the reference permeability is increased ten times ($10^{-17}m^2$), the pulsing response totally vanishes, leading to a steady state flow (Figure 17, curve 'h'). Indeed, the permeability increase prevents the low-permeability layer from slowing down gas migration through it, leading to a lack of pressure variation within the lower draining part of the fault.

3.2.5 Contribution of the thickness of the low-permeability layer

While keeping the same depth for the bottom of the low-permeability layer, we increased its thickness from 50 m for the reference case to 100 m and 150 m

(Figure 18, bottom). As the reference thickness of the low-permeability layer is doubled, the pulse periodicity increases slightly from 90-100 days to 100-150 days (case 'e' for a 100 m-thick layer). However, when further increasing the low-permeability layer's thickness to 150 m (case 'f'), one can observe a damped signal at the surface resulting in the disappearance of the H_2 pulses. The longer path needed for the gas to cross the impermeable layer increases dramatically the time required to escape fast enough to close it (Figure 18, curve 'f' with longer pulsing time). Indeed, the fluid pressure in the lower drained zone remains high enough to keep the lower part of the impermeable layer open.

3.3 Discussion

Table 7 summarizes the results of this parametric study by sorting the different simulations according to the flow rate regime of H_2 at the surface. The results exhibiting a constant, i.e. steady state, H_2 flow rate at the surface present specific characteristics. First, simulations r, k, d, n and o that resulted in damped or steady surface H_2 flows yield maximum initial effective stress values inside the lower part of the low-permeability zone below 8 MPa (red cells for the effective stress values) during the gas pressure loading stage, while simulations resulting in pulsing regimes of H_2 show a higher initial effective stress. Second, no pulse is observed when the permeability of the low-permeability layer is too high (here 2×10^{-17} m^2 for simulations m and h; red cells for the residual permeability of the low-permeability layer), meaning that a permeability contrast of at least four orders of magnitude is required to generate H_2 pulses. Finally, and as seen previously, an extreme incoming flow rate of H_2 (simulations j and p; red cells with an 842 Kmol/day value) induces a constant aperture of the low-permeability zone and a constant outcoming flow of H_2 at the surface.

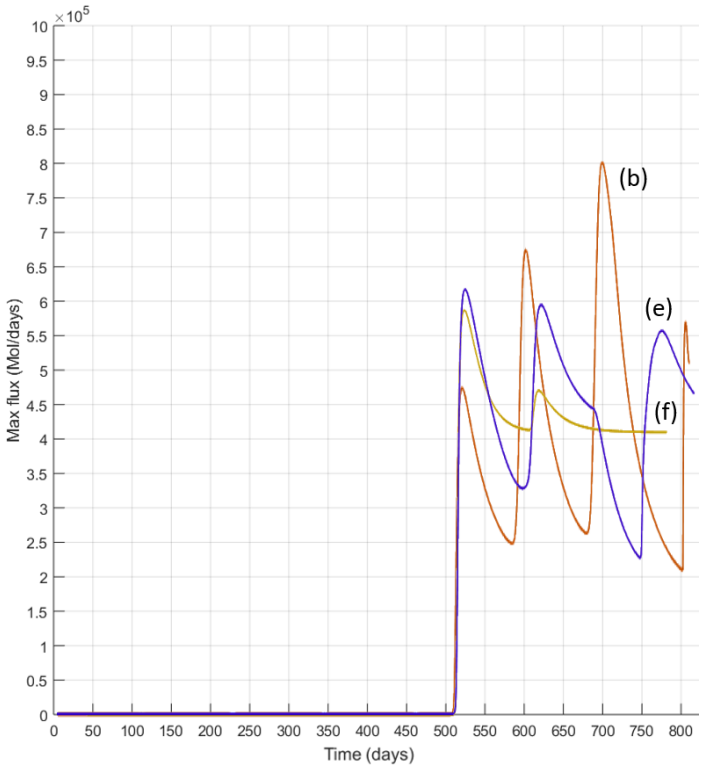

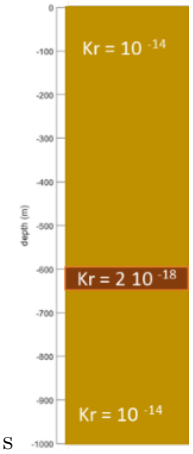

s ref case (b)

Figure 18. Resulting flow rates at the surface for three different thicknesses of the low-permeability layer: i.e.

Table 7. Summary of the performed simulations, including the initial conditions and the simulation results ("

Table 7. Summary of the performed simulations, including the initial conditions and the simulation results ("

Simulation ID
a
b (ref case)
g
i
e
s*
q
c
f
l
j
p
r
k
m
h
d
n
o

This parametric study highlights three main conditions essential to obtain a sustainable H_2 pulse system at the surface (dark green cells lines):

- a low permeability value for the low-permeability layer, here $< 10^{-18}$ m^2;
- a low incoming flow rate of H_2 at the bottom of the fault, here $<$ 842 Kmol/day;
- a high initial effective stress value at the bottom of the low permeable layer, here around 8 MPa.

These conditions are also observed in the configurations resulting in slightly damped H_2 pulses with an initial effective stresses are around 8 MPa, i.e. where the fluid pressure is initially low (light green cells in Table 7). This means that secondary order parameters contribute to the sustainability of surface H_2 pulse systems here, e.g. H_2 gas compressibility, however not impacting the main trend of the results. One can note that these main required conditions to generate pulses are strongly linked to the formulation of the relationship between the permeability and the effective stress (equations 32-37). It is an important increase of the fluid pressure in an initially low permeable medium which leads to a "valve-fault" response. This response is characterized by an alternation of aperture-closure sequences of the low-permeability layer. We present a conceptual model summarizing our conclusions regarding the flow rate regime of H_2 at the surface depending on permeability *versus* effective stress in

Figure 19.

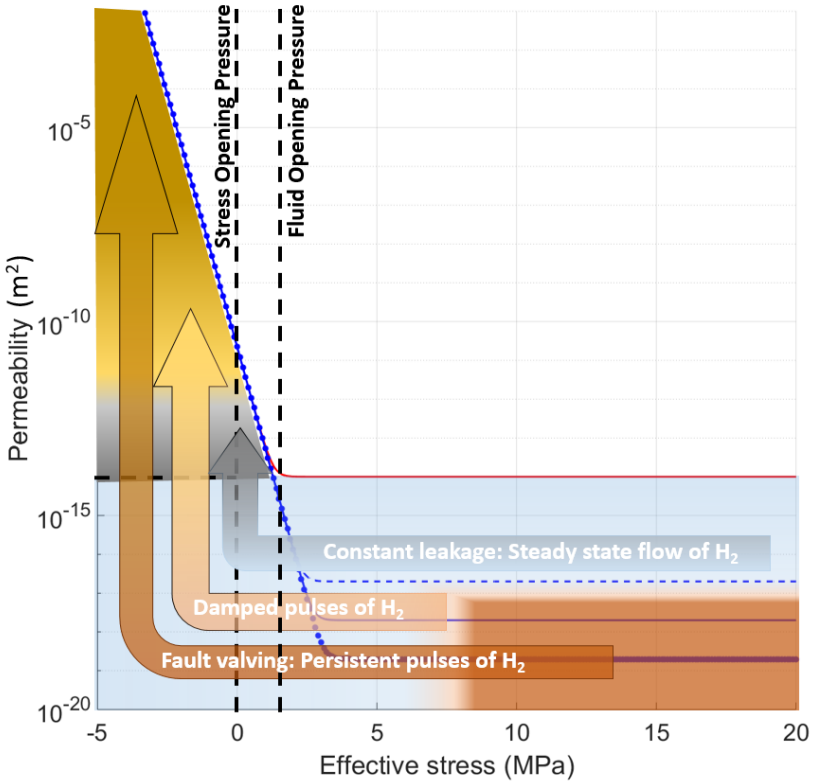

Figure 19. Conceptual model summarizing the results of the full set of numerical simulations.

In order to check if this model can be used to predict H_2 flow rate regime at the surface with a different set of parameters, we consider a different tectonic stress-environment. We use a stress ratio between the vertical and horizontal stress of 1 instead of the previously used stress ratio of 0.6 which corresponds to an extensive tectonic regime. We apply a stress ratio of 1 to the extreme case 'd' that resulted in a rather constant regime with no pulsing peak generated at the surface (case s* in Table 7, the dark blue cell line). A pulsing regime is now obtained (dark blue curve in Figure 20) with sharp peaks that exhibit higher peak intensity and larger periodicity of the flow rate (150 to 240 days for case 's*') compared to the reference case 'b' (90-100 days).

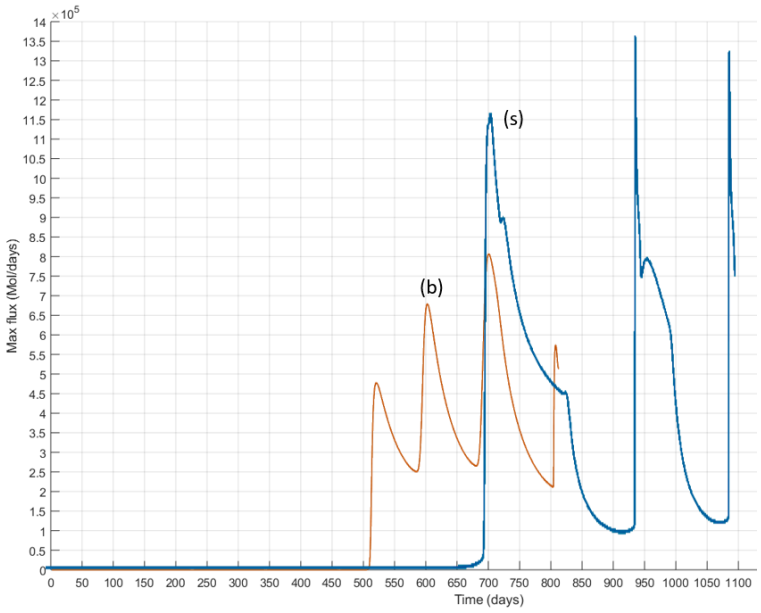

Figure 20. Resulting flow rates at the surface for the predicted case s* for which $_{\mathbf{h}}= \ _{\mathbf{V}}$ (dark blue curve 's')

4. Conclusions

We set up a numerical model in the MRST framework to study fluid migration in a vertical 2D planar fault. We focus on H_2O and H_2 migration and for that, we proposed a set of equations including state equations to be used as mass and energy conservation equations. We consider the fault draining part, i.e. the damage zone and its interface with the core zone, as an equivalent porous medium, allowing us to use the Darcy law to characterize the fluid flow. To verify the validity of the numerical model, we first simulate the morphology and amplitude of 2D thermal anomalies induced by buoyancy-driven water flow that eventually match the results obtained by Guillou-Frottier et al. (2020). Then, we focus on various geomechanic parameters that control a H_2 pulsing regime at the surface along a valve-fault system at depth. We neglect the coupling terms between liquid water and gaseous H_2 to consider only gas migration since H_2 solubility is very low on the last 1000 m along the fault and below the surface. The fault-valve system can be generated in presence of a low-permeability layer obstructing the migration path along the fault, whose permeability depends on the in-situ effective stress as defined by equations 32-37 (Donzé et al. 2020a). This parametric study highlights essential conditions for the generation of a pulsing flow rate of H_2 at the surface: (i) a high permeability contrast between the low-permeability and the draining parts of the fault, (ii) a sufficiently high initial effective stress value at the bottom of the impermeable layer; (iii) an

incoming H_2 flow rate at the fault base lower than a critical value in order to avoid a constant aperture of the low permeable layer, annihilating the valve-fault mechanism.

In simulations resulting in pulsing H_2 flows, the obtained pulsing periodicity ranges from 100 to 300 days. Recent long-term monitoring campaigns installed a high density of permanent H_2 detectors in two structures in the Minas Gerais State (Brazil) recorded two kinds of signals : large sporadic pulses affecting the soil H_2 content for one or two days, and smaller ones with a daily periodicity that last for 6 h (Moretti et al., 2021). According to our model, such pulse periodicities are too short to be explained by a fault-valve system at depth. Indeed, the formulation permeability-effective stress could provide an overestimation of the permeability since it has been formulated from experiments carried out below depths of -300 m deep and cannot be used for shallower depths (above -200 m). Unfortunately, permanent gas detectors along draining faults are not systematic yet. The only long term monitoring H_2 release from a rock mass during several years with a daily frequency has been performed by Nivin (2019) in an underground mine in the Lovozero loparite deposit. It was shown that barogenic (atmospheric pressure variation) and human-induced (technogenic explosions) factors were the most important in defining the dynamics of H_2 emanation. To go further, we expect several arrays of detectors to be deployed along tectonic faults in the coming years. H_2 bursts periodicities detected at the time scale of a few months could then become the expression of an actively filled reservoir of native H_2 at depth.

Acknowledgments

Lukas Bourdet would like to thank INP – Institut Polytechnique Grenoble (internship n° 72567). Part of the work has been financially supported by the French National Research Agency (ANR) through the H2KOLA project (ANR-20 – CE01-0020 – H2KOLA) as well as the Laboratoire ISTerre (cross-cutting themes grant, “BQR”).

References

- Achtziger-Zupančič, P., Loew, S., & Hiller, A. (2017). Factors controlling the permeability distribution in fault vein zones surrounding granitic intrusions (Ore Mountains/Germany). Journal of Geophysical Research: Solid Earth, 122(3), 1876-1899.
- Bazarkina, E. F., Chou, I. M., Goncharov, A. F., & Akinfiev, N. N. (2020). The behavior of H_2 in aqueous fluids under high temperature and pressure. Elements: An International Magazine of Mineralogy, Geochemistry, and Petrology, 16(1), 33-38.
- Beinlich, A., Austrheim, H., Mavromatis, V., Grguric, B., Put-

nis, C. V., & Putnis, A. (2018). Peridotite weathering is the missing ingredient of Earth's continental crust composition. Nature communications, 9(1), 1-12.

- Bonté, D., Guillou-Frottier, L., Garibaldi, C., Bourgine, B., Lopez, S., Bouchot, V., & Lucazeau, F. (2010). Subsurface temperature maps in French sedimentary basins: new data compilation and interpolation. Bulletin de La Société Géologique de France, 181(4), 377–390.
- Cannat, M., Fontaine, F., & Escartin, J. (2010). Serpentinization and associated hydrogen and methane fluxes at slow spreading ridges. Book Series:Geophysical Monograph Series, Editors: Peter A. Rona, Colin W. Devey, Jérôme Dyment, Bramley J. Murton, Geophysical Monograph Series 188:241-264
- Chabab, S., Theveneau, P., Coquelet, C., Corvisier, J., & Paricaud, P. (2020). Measurements and predictive models of high-pressure H2 solubility in brine (H2O+ NaCl) for underground hydrogen storage application. International Journal of Hydrogen Energy, 45(56), 32206-32220.
- Collignon, M., Klemetsdal, Ø. S., Møyner, O., Alcanié, M., Rinaldi, A. P., Nilsen, H., & Lupi, M. (2020). Evaluating thermal losses and storage capacity in high-temperature aquifer thermal energy storage (HT-ATES) systems with well operating limits: Insights from a study-case in the Greater Geneva Basin, Switzerland. Geothermics, 85, 101773.
- Donzé, F. V., Tsopela, A., Guglielmi, Y., Henry, P., & Gout, C. (2020a). Fluid migration in faulted shale rocks: channeling below active faulting threshold. European Journal of Environmental and Civil Engineering, 1-15.
- Donzé, F. V., Truche, L., Shekari Namin, P., Lefeuvre, N., & Bazarkina, E. F. (2020b). Migration of natural hydrogen from deep-seated sources in the São Francisco Basin, Brazil. Geosciences, 10(9), 346.
- Duan, Q., & Yang, X. (2014). Experimental studies on gas and water permeability of fault rocks from the rupture of the 2008 Wenchuan earthquake, China. Science China Earth Sciences, 57(11), 2825-2834.
- Ellison, E. T., Templeton, A. S., Zeigler, S. D., Mayhew, L. E., Kelemen, P. B., Matter, J. M., & Oman Drilling Project Science Party. (2021). Low-Temperature Hydrogen Formation During Aqueous Alteration of Serpentinized Peridotite in the Samail Ophiolite. Journal of Geophysical Research: Solid Earth, 126(6).

- Faulkner, D. R., Jackson, C. A. L., Lunn, R. J., Schlische, R. W., Shipton, Z. K., Wibberley, C. A. J., & Withjack, M. O. (2010). A review of recent developments concerning the structure, mechanics and fluid flow properties of fault zones. Journal of Structural Geology, 32(11), 1557–1575.
- Florence, F. A., Rushing, J., Newsham, K. E., & Blasingame, T. A. (2007). Improved permeability prediction relations for low permeability sands. In Rocky mountain oil & gas technology symposium.
- Fossen, H. (2020). Chapter 8 - Fault classification, fault growth, and displacement. Elsevier.
- Frery, E., Langhi, L., Maison, M., & Moretti, I. (2021). Natural hydrogen seeps identified in the North Perth Basin, Western Australia. International Journal of Hydrogen Energy.
- Giampiccolo, E., Brancato, A., Manuella, F. C., Carbone, S., Gresta, S., & Scribano, V. (2017). New evidence for the serpentinization of the Palaeozoic basement of southeastern Sicily from joint 3-D seismic velocity and attenuation tomography. Geophysical Journal International, 211(3), 1375-1395.
- Ghanizadeh, A., Amann-Hildenbrand, A., Gasparik, M., Gensterblum, Y., Krooss, B. M., & Littke, R. (2014). Experimental study of fluid transport processes in the matrix system of the European organic-rich shales: II. Posidonia Shale (Lower Toarcian, northern Germany). International Journal of Coal Geology, 123, 20-33.
- Gilat, A. L. & Vol, A. (2012). Degassing of primordial hydrogen and helium as the major energy source for internal terrestrial processes. Geoscience Frontiers, 3(6), 911-921.
- Guillou-Frottier, L., Duwiquet, H., Launay, G., Taillefer, A., Roche, V., & Link, G. (2020). On the morphology and amplitude of 2D and 3D thermal anomalies induced by buoyancy-driven flow within and around fault zones. Solid Earth, 11(4), 1571-1595.
- Hainzl, S. (2004). Seismicity patterns of earthquake swarms due to fluid intrusion and stress triggering. Geophysical Journal International, 159(3), 1090–1096.
- Hardebeck, J. L. (2012). Fluid-Driven Seismicity Response of the Rinconada Fault near Paso Robles, California, to the 2003 M 6.5 San Simeon Earthquake.
- Henry, P., Guglielmi, Y., Gout, C., Castilla, R., Dick, P., Donzé, F., Tsopela, A., Neyens, D., De Barros, L., & Durand, J. (2019,

September). Strain and flow pathways in a shale fault zone: An in-situ test of fault seal integrity. In Fifth International Conference on Fault and Top Seals (Vol. 2019, No. 1, pp. 1-5). European Association of Geoscientists & Engineers.

- Kietäväinen, R., Ahonen, L., Kukkonen, I.T., Hendriksson, N., Nyyssönen, M. and Itävaara, M. (2013). Characterisation and isotopic evolution of saline waters of the Outokumpu Deep Drill Hole, Finland–Implications for water origin and deep terrestrial biosphere. Applied geochemistry, 32, pp.37-51.
- Klinkenberg, L. J. (1941). The permeability of porous media to liquids and gases. Am. Petrol. Inst., Drilling and Production Practice, 2, 200-213.
- Larin, N., Zgonnik, V., Rodina, S., Deville, E., Prinzhofer, A., Larin, V.N. (2015). Natural molecular hydrogen seepage associated with surficial, rounded depressions on the European craton in Russia. Natural Resources Research, 24(3), 369-383.
- Lauser, A., Hager, C., Helmig, R., & Wohlmuth, B. (2011). A new approach for phase transitions in miscible multi-phase flow in porous media. Advances in Water Resources, 34(8), 957-966.
- Lefeuvre, N., Truche, L., Donzé, F. V., Ducoux, M., Barré, G., Fakoury, R. A., Calassou, S. & Gaucher, E. C. (2021). Native H_2 exploration in the western Pyrenean foothills. Geochemistry, Geophysics, Geosystems. 22(8).
- Lefeuvre, N., Truche, L., Donzé, F. V., Gal, F., Tremosa, J., Fakoury, R. A., Calassou, S., & Gaucher, E. (2022). Natural hydrogen migration along thrust faults in foothill basins: The North Pyrenean Frontal Thrust case study. Applied Geochemistry, 145, 105396.
- Lemmon, E. W., Huber, M. L., & Leachman, J. W. (2008). Revised standardized equation for hydrogen gas densities for fuel consumption applications. Journal of Research of the national Institute of Standards and Technology, 113(6), 341.
- Lie, K. A. (2019). An introduction to reservoir simulation using MATLAB/GNU Octave: User guide for the MATLAB Reservoir Simulation Toolbox (MRST). Cambridge University Press.
- Lin, L.H., Hall, J., Lippmann-Pipke, J., Ward, J.A., Sherwood Lollar, B., DeFlaun, M., Rothmel, R., Moser, D., Gihring, T.M., Mislowack, B., … & Onstot. T.C. (2005). Radiolytic H_2 in continental crust: Nuclear power for deep subsurface microbial communities. Geochemistry, Geophysics, Geosystems, 6(7).

- Linstrom, P. J. and Mallard, W. G. (2001), The NIST Chemistry WebBook: a chemical data resource on the internet, J. Chem. Eng. Data, 46, 1059–1063.
- Ménez, B. (2020). Abiotic hydrogen and methane: fuels for life. Elements: An International Magazine of Mineralogy, Geochemistry, and Petrology, 16(1), 39-46.
- Monnin, C., Quéméneur, M., Price, R., Jeanpert, J., Maurizot, P., Boulart, C., Donval, J.P., & Pelletier, B. (2021). The chemistry of hyperalkaline springs in serpentinizing environments: 1. the composition of free gases in New Caledonia compared to other springs worldwide. Journal of Geophysical Research: Biogeosciences. 126(9).
- Moretti, I., Prinzhofer, A., Françolin, J., Pacheco, C., Rosanne, M., Rupin, F., & Mertens, J. (2021). Long-term monitoring of natural hydrogen superficial emissions in a brazilian cratonic environment. Sporadic large pulses versus daily periodic emissions. International Journal of Hydrogen Energy, 46(5), 3615-3628.
- Muzny, C. D., Huber, M. L., & Kazakov, A. F. (2013). Correlation for the viscosity of normal hydrogen obtained from symbolic regression. Journal of Chemical & Engineering Data, 58(4), 969-979.
- Myagkiy, A., Brunet, F., Popov, C., Krüger, R., Guimarães, H., Sousa, R. S., Charlet, L., & Moretti, I. (2020). H2 dynamics in the soil of a H_2-emitting zone (São Francisco Basin, Brazil): Microbial uptake quantification and reactive transport modelling. Applied Geochemistry, 112, 104474.
- Nivin, V. A. (2019). Occurrence forms, composition, distribution, origin and potential hazard of natural hydrogen–hydrocarbon gases in ore deposits of the Khibiny and Lovozero Massifs: a review. Minerals, 9(9), 535.
- Palliser, C., & McKibbin, R. (1998). A model for deep geothermal brines, I: TpX state-space description. Transport in porous media, 33(1), 65-80.
- Pan, B., Yin, X., Ju, Y., & Iglauer, S. (2021). Underground hydrogen storage: Influencing parameters and future outlook. Advances in Colloid and Interface Science, 294, 102473.
- Peng, S. (2021). Advanced understanding of gas flow and the Klinkenberg effect in nanoporous rocks. Journal of Petroleum Science and Engineering, 206, 109047.
- Prinzhofer, A.; Moretti, I.; Francolin, J.; Pacheco, C.; d'Agostino, A.; Werly, J.; Rupin, F. (2019) Natural hydrogen

continuous emission from sedimentary basins: The example of a Brazilian H_2-emitting structure. Int. J. Hydrogen Energy, 44, 5676–5685.

- Rabinowicz, M., Boulegue, J., & Genthon, P. (1998). Two-and three-dimensional modeling of hydrothermal convection in the sedimented Middle Valley segment, Juan de Fuca Ridge. Journal of Geophysical Research: Solid Earth, 103(B10), 24045-24065.
- Rowland, J. V., & Sibson, R. H. (2004). Structural controls on hydrothermal flow in a segmented rift system, Taupo Volcanic Zone, New Zealand. Geofluids, 4(4), 259-283.
- Seward, T. M., & Franck, E. U. (1981). The system hydrogen-water up to 440 C and 2500 bar pressure. Berichte der Bunsengesellschaft für physikalische Chemie, 85(1), 2-7.
- Sherwood Lollar, B.S., Onstott, T.C., Lacrampe-Couloume, G. and Ballentine, C.J. (2014). The contribution of the Precambrian continental lithosphere to global H2 production. Nature, 516(7531), 379-382.
- Souriau, A., Rigo, A., Sylvander, M., Benahmed, S., & Grimaud, F. (2014). Seismicity in central-western Pyrenees (France): A consequence of the subsidence of dense exhumed bodies. Tectonophysics, 621, 123-131.
- Sylvander, M., Rigo, A., Sénéchal, G., Battaglia, J., Benahmed, S., Calvet, M., Chevrot. S., Douchain, J.M., Grimaud, F., Letort, J., & Pauchet, H. (2021). Seismicity patterns in southwestern France. Comptes Rendus. Géoscience, 353(S1), 79-104.
- Taillefer, A., Soliva, R., Guillou-Frottier, L., Le Goff, E., Martin, G., & Seranne, M. (2017). Fault-related controls on upward hydrothermal flow: an integrated geological study of the Têt fault system, Eastern Pyrénées (France). Geofluids, 2017.
- Tarling, M. S., Smith, S. A., & Scott, J. M. (2019). Fluid overpressure from chemical reactions in serpentinite within the source region of deep episodic tremor. Nature Geoscience, 12(12), 1034-1042.
- Tsopela, A., Donzé, F. V., Guglielmi, Y., Castilla, R., & Gout, C. (2019). Hydromechanical reactivation of natural discontinuities: mesoscale experimental observations and DEM modeling. Acta Geotechnica, 14(5), 1585-1603.
- Truche, L., Berger, G., Destrigneville, C., Pages, A., Guillaume, D., Giffaut, E., & Jacquot, E. (2009). Experimental reduction of aqueous sulphate by hydrogen under hydrothermal conditions:

implication for the nuclear waste storage. Geochimica et Cosmochimica Acta, 73(16), 4824-4835.

- Truche, L., Berger, G., Destrigneville, C., Guillaume, D., & Giffaut, E. (2010). Kinetics of pyrite to pyrrhotite reduction by hydrogen in calcite buffered solutions between 90 and 180 C: Implications for nuclear waste disposal. Geochimica et Cosmochimica Acta, 74(10), 2894-2914.
- Truche, L., Jodin-Caumon, M. C., Lerouge, C., Berger, G., Mosser-Ruck, R., Giffaut, E., & Michau, N. (2013). Sulphide mineral reactions in clay-rich rock induced by high hydrogen pressure. Application to disturbed or natural settings up to 250 C and 30 bar. Chemical Geology, 351, 217-228.
- Truche, L., Joubert, G., Dargent, M., Martz, P., Cathelineau, M., Rigaudier, T., & Quirt, D. (2018). Clay minerals trap hydrogen in the Earth's crust: evidence from the Cigar Lake uranium deposit, Athabasca. Earth and Planetary Science Letters, 493, 186-197.
- Truche, L., McCollom, T.M. & Martinez, I. (2020). Hydrogen and abiotic hydrocarbons: molecules that change the world. Elements: An International Magazine of Mineralogy, Geochemistry, and Petrology, 16(1), 13-18.
- Truche, L., Donzé, F.V., Dusséauxe, C., Pages, A., Lefeuvre, N., Brunet, F., & Malvoisin, B. (2022). The quest for native hydrogen: new directions for exploration ("à la recherche de l'hydrogène natif: de nouvelles orientations pour l'exploration"), Géologues, géosciences et société, ISSN 0016.7916, N° 213, June 2022, 68-73
- Yang, D., Wang, W., Chen, W., Wang, S., & Wang, X. (2017). Experimental investigation on the coupled effect of effective stress and gas slippage on the permeability of shale. Scientific Reports, 7(1), 1-9.
- Wibberley, C. A., Yielding, G., & Di Toro, G. (2008). Recent advances in the understanding of fault zone internal structure: a review. Geological Society, London, Special Publications, 299(1), 5-33.
- Yekta, E. (2017). Characterization of geochemical interactions and migration of hydrogen in sandstone sedimentary formations: application to geological storage (Doctoral dissertation, Université d'Orléans).
- Yu, I., Klyukin, Y. I., Lowell, R. P., & Bodnar, R. J. (2017). A revised empirical model to calculate the dynamic viscosity of

H2ONaCl fluids at elevated temperatures and pressures (1000° C, 500 MPa, 0–100 wt% NaCl). Fluid Phase Equilibria, 433, 193-205.

- Zgonnik, V., Beaumont, V., Deville, E., Larin, N., Pillot, D., & Farrell, K.M. (2015) Evidence for natural molecular hydrogen seepage associated with Carolina bays (surficial, ovoid depressions on the Atlantic Coastal Plain, Province of the USA). Progress in Earth and Planetary Science. 2(1), 1-15.
- Zgonnik, V. (2020). The occurrence and geoscience of natural hydrogen: A comprehensive review. Earth-Science Reviews, 203, 103140.
- Zhang, L., Nasika, C., Donzé, F. V., Zheng, X., Renard, F., & Scholtès, L. (2019). Modeling porosity evolution throughout reaction-induced fracturing in rocks with implications for serpentinization. Journal of Geophysical Research: Solid Earth, 124(6), 5708-5733.
- Zheng, J., Zheng, L., Liu, H. H., & Ju, Y. (2015). Relationships between permeability, porosity and effective stress for low-permeability sedimentary rock. International Journal of Rock Mechanics and Mining Sciences, 78, 304-318.
- Zheng, X., Cordonnier, B., Zhu, W., Renard, F., & Jamtveit, B. (2018). Effects of confinement on reaction-induced fracturing during hydration of periclase. Geochemistry, Geophysics, Geosystems, 19(8), 2661-2672.